

Disentangling correlated scatter in cluster mass measurements

Yookyung Noh¹ and J.D. Cohn²

¹ *Department of Astronomy and Theoretical Astrophysics Center, University of California, Berkeley, CA 94720*

² *Space Sciences Laboratory and Theoretical Astrophysics Center, University of California, Berkeley, CA 94720*

2 March 2013

ABSTRACT

The challenge of obtaining galaxy cluster masses is increasingly being addressed by multiwavelength measurements. As scatters in measured cluster masses are often sourced by properties of or around the clusters themselves, correlations between mass scatters are frequent and can be significant, with consequences for errors on mass estimates obtained both directly and via stacking. Using a high resolution $250h^{-1}Mpc$ side N-body simulation, combined with proxies for observational cluster mass measurements, we obtain mass scatter correlations and covariances for 243 individual clusters along ~ 96 lines of sight each, both separately and together. Many of these scatters are quite large and highly correlated. We use principal component analysis (PCA) to characterize scatter trends and variations between clusters. PCA identifies combinations of scatters, or variations more generally, which are uncorrelated or non-covariant. The PCA combination of mass measurement techniques which dominates the mass scatter is similar for many clusters, and this combination is often present in a large amount when viewing the cluster along its long axis. We also correlate cluster mass scatter, environmental and intrinsic properties, and use PCA to find shared trends between these. For example, if the average measured richness, velocity dispersion and Compton decrement mass for a cluster along many lines of sight are high relative to its true mass, in our simulation the cluster's mass measurement scatters around this average are also high, its sphericity is high, and its triaxiality is low.

Our analysis is based upon estimated mass distributions for fixed true mass. Extensions to observational data would require further calibration from numerical simulations, tuned to specific observational survey selection functions and systematics.

Key words: Cosmology: theory, large-scale structure of the Universe

1 INTRODUCTION

Although there is no question that galaxy clusters are the most massive virialized objects in the Universe, identifying the mass of any particular cluster remains a challenge. A cluster's mass is however one of its core properties, important for using cluster samples statistically to constrain cosmological parameters, for understanding clusters as hosts for galaxy evolution, and for studying the growth and other properties of the clusters themselves. Recent reviews include Voit (2005); Borgani (2008); Myers et al. (2009); Allen, Evrard & Mantz (2011).

In simulations, the cluster mass is the sum of the masses of the simulation particles which are cluster members, for whatever cluster member (and thus mass) definition is used (comparisons of some mass definitions are found in, e.g., White (2001, 2002); Hu & Kravtsov (2003); Cuesta et al. (2008); Lukic et al. (2009)). From a given cosmological set of parameters, simulations predict well defined and directly

measurable masses, accurate to the extent that the simulation captures the required physics and has the requisite resolution. These theoretical mass definitions cannot be directly applied to observational data, as observations instead measure properties of galaxies both within the cluster and near the cluster, or gas within and sometimes near the cluster, or the bending of space by mass in and around the cluster. These observational mass proxies are converted, via physical modeling and assumptions, to mass measurements for comparison with theory. Improvements in the noisy mappings between observationally accessible cluster properties and theoretically calculable cluster properties is much sought after by both theorists and observers. Complications for observations include projection (and more generally the lack of three dimensional information¹) and reliance of the mapping

¹ There is a long history, e.g. for optical cluster richness starting with Abell (1958) and continuing with, for example,

between mass and observational proxy upon simplifying assumptions such as hydrostatic equilibrium. The simulation based theoretical approaches, for their part, find it challenging to capture the directly observable baryonic physics, including galaxy properties.

In order to alleviate systematics and reduce errors in observationally obtained cluster masses, it is becoming common to combine measurements from different (often multiwavelength) observational techniques. The advantages of complementary information and crosschecks are unfortunately mitigated by the fact that scatters from different observational methods are often correlated. Essentially, as physical properties of the clusters themselves and their environments are often the causes of mass measurement scatters, more than one measurement technique can be affected. It is important include these correlations in order to properly estimate the errors in mass measurements of any individual cluster and to avoid a bias when stacking clusters on one property and measuring another. (For discussion see Rykoff et al. (2008); Cohn & White (2009); Stanek et al. (2010); White, Cohn & Smit (2010), additional simulated examples of correlated scatters using different observational methods include Meneghetti et al. (2010); Rasia et al. (2012); analyses are beginning to include these, e.g. Rozo et al. (2009); Mantz et al. (2010); Benson et al. (2011).). A recent application to an observational cluster sample, resolving some questions raised by earlier analyses is found in Angulo et al. (2012).)

Here we consider multiwavelength mass measurements for clusters “observed” in a cosmological dark matter simulation. Our primary focus is on mass scatters for individual clusters viewed along several different lines of sight. We measure and characterize the multiwavelength correlations and covariances, and study their relation to other cluster properties using both correlations and PCA, principal component analysis. This extends recent work using PCA to compare relationships between cluster (Skibba & Maccio 2011; Jeesson-Daniel et al. 2011) properties such as concentration, mass and ellipticity in simulations, and some supercluster counterparts, Einasto et al. (2011, 2012), in observations.²

The mass observables we simulate are red galaxy richness, phase space richness, velocity dispersions, Sunyaev-

Zel’dovich decrement and weak lensing ζ statistic (Fahlman et al. 1994; Kaiser 1995), techniques in use or planned for large volume current and upcoming cluster surveys such as Atacama Cosmology Telescope (ACT³), South Pole Telescope (SPT⁴), Blanco Cosmology Survey (BCS⁵), Dark Energy Survey (DES⁶) and Large Synoptic Survey Telescope (LSST⁷).

The mock simulation measurements, their scatters, and general information about PCA are in §2. (Much of §2 summarizes work on the same simulation detailed in White, Cohn & Smit (2010) (hereafter WCS), and further studied in Noh & Cohn (2011) and Cohn (2011).) In §3, mass scatters for each cluster, along ~ 96 lines of sight, are correlated, and their covariances are analyzed via PCA. Distributions of the scatter properties are considered, and, cluster by cluster, the PCA direction of largest scatters is compared to special physical cluster directions. In §4 cluster properties, including the individual cluster mass scatter distributions, and environmental and intrinsic properties, are intercompared using correlations and PCA. In §5 PCA is instead applied to mass scatter for the whole sample of clusters at once, to analyze scatter including both line of sight and cluster-to-cluster variation, with some discussion of possible extensions to observations. §6 discusses outliers and §7 summarizes.

While we were preparing this work for publication, Angulo et al. (2012) appeared. They consider correlated mass scatter in multiwavelength measurements, in a 4.1 Gpc side simulation which also includes X-ray.

2 SIMULATIONS AND METHODS

2.1 N-body data

Our simulation data are the outputs of an N-body simulation of M. White, described in detail in WCS. His TreePM (White 2002) code was run with 2048³ particles in a periodic box with side length 250 $h^{-1}Mpc$. The 45 outputs are equally spaced in $\ln(a)$ from $z = 10$ to $z = 0$. Cosmological parameters were taken to be $(h, n, \Omega_m, \sigma_8) = (0.7, 0.95, 0.274, 0.8)$, consistent with a large number of cosmological observations. We focus here on mock observations at $z = 0.1$, where our methods have been most closely tuned to and tested with observational data, as reported in WCS. Halos are found via Friends of Friends (FoF) (Davis et al. 1985), with linking length $b = 0.168$ times the mean inter-particle spacing (connecting regions with density at least roughly 100 times the mean background density). Clusters are halos with FoF masses $M \geq 10^{14} h^{-1} M_\odot$ (M hereon will mean this $b = 0.168$ FoF mass, we will also write this as M_{true} when comparing to estimates). There are 243 clusters in the box. Note that because we have a periodic box we do not need to worry about clusters located near the edge, similarly, because we are using FoF as a halo finder, every particle is uniquely assigned to a single halo.

Dalton et al. (1992); Lumsden et al. (1992); van Haarlem et al. (1997); White et al. (1999); Cohn, Evrard, White et al. (2007); Cohn & White (2009); Rozo et al. (2011); Biesiadzinski et al. (2012), for cluster weak lensing (e.g., Reblinsky & Bartelmann (1999); Metzler, White & Loken (2001); Hoekstra (2001); de Putter & White (2005); Meneghetti et al. (2010); Becker & Kravtsov (2011); Hoekstra et al. (2011)), for cluster Sunyaev-Zel’dovich (Sunyaev & Zel’dovich 1972, 1980) (SZ) flux measurements, (e.g., White, Hernquist & Springel (2002); Holder, McCarthy & Babul (2007); Hallman et al. (2007); Shaw, Holder & Bode (2008); Angulo et al. (2012)) and for cluster velocity dispersions (e.g., Cen (1997); Tormen (1997); Kasun & Evrard (2005); Biviano et al. (2006); White, Cohn & Smit (2010); Saro et al. (2012)).

² Comparing cluster mass scatters to physical cluster properties has a long history, recent studies include Yang, Bhattacharya & Ricker (2010); Becker & Kravtsov (2011); Battaglia, Bond, Pfrommer & Sievers (2011); Bahe, McCarthy & King (2012), as well as papers mentioned above.

³ www.physics.princeton.edu/act/

⁴ pole.chicago.edu

⁵ cosmology.uiuc.edu/BCS/

⁶ www.darkenergysurvey.org

⁷ www.lsst.org/

Galaxies are taken to be resolved subhalos, which are found via Fof6d (Diemand, Kuhlen & Madau 2006), with the implementation as described in the appendix of WCS. Subhalos are tracked (see Wetzel, Cohn & White (2009); Wetzel & White (2010) for particular details) from their infall into their host halos in order to assign luminosities via subhalo abundance matching (Conroy, Wechsler & Kravtsov 2006). The resulting galaxy catalogue minimum luminosity at $z = 0.1$ is $0.2L_*$ (again see WCS for more discussion and validation tests of the catalogue galaxy properties with observations).

2.2 Cluster mass measurements and scatters

We consider five cluster mass measurement methods with this simulation (see WCS for specifics):

- N_{red} : Richness using the Koester et al. (2007) MaxBCG algorithm based upon colors. Galaxy colors are assigned using the algorithm of Skibba & Sheth (2009) with evolution of Conroy, Gunn & White (2009); Conroy, White, & Gunn (2010); Conroy, & Gunn (2010). Galaxies are taken to be “red” if they have $g - r$ within 0.05 of the peak of the red galaxy $g - r$ distribution specified by Skibba & Sheth (2009) for their observed M_r , again see WCS for more detail.

- N_{ph} : Richness based upon spectroscopy, with cluster membership assigned via the criteria of Yang, Mo & van den Bosch (2007).

- SZ: SZ flux (Compton decrement) is assigned to every particle by giving it a temperature based upon the mass of its halo. For every cluster, its measured SZ flux is then the flux within an annulus of radius r_{180b} (the radius within which the average mass is greater than or equal to 180 times background density), through the length of the box, apodized at the edges. This was shown in e.g. White, Hernquist & Springel (2002) to well approximate hydrodynamic simulation results for SZ at the scales appropriate for two cluster surveys mentioned earlier, SPT and ACT.

- Vel: Velocity dispersions calculated via the method detailed in WCS, and based on den Hartog & Katgert (1996); Biviano et al. (2006); Wojtak et al. (2007). Phase space information is used to reject outliers and the mass estimate includes the harmonic radius (calculated as part of the outlier rejection, more details and definitions in WCS).

- WL: Weak lensing using a singular isothermal sphere (SIS) or NFW model to assume a cluster lens profile and then fitting the projected mass, using the ζ statistic (Fahlman et al. 1994; Kaiser 1995), in a cylinder with radius r_{180b} and (apodized) length of the box (again WCS describes fitting models, etc.).

The red galaxy richness, phase space richness and velocity dispersions measured in our simulations are expected to include the majority of systematics that are present in real observations. The weak lensing and Compton decrement (SZ) observations however do not include all known systematics, such as miscentering, shape measurement and source redshift errors for lensing, and foreground and point source removal for Compton decrement. The relatively small box size ($250 h^{-1} \text{Mpc}$ on a side) also means that line of sight scatter is underestimated (e.g., White, Hernquist & Springel (2002); Hallman et al. (2007); Holder, McCarthy & Babul (2007); Cohn & White (2009);

Angulo et al. (2012) for SZ and Reblinsky & Bartelmann (1999); Metzler, White & Loken (2001); Hoekstra (2001); de Putter & White (2005); Meneghetti et al. (2010); Becker & Kravtsov (2011); Bahe, McCarthy & King (2012); Hoekstra et al. (2011) for lensing).

We extend the cluster sample used in WCS to a lower mass range, $M \geq 10^{14} h^{-1} M_\odot$, as in Noh & Cohn (2011); Cohn (2011). The five observables listed above are found along 96 lines of sight for each cluster, each time placing the cluster at the center of the periodic box. Just as in WCS, lines of sight for clusters are removed for all measurement methods when a more massive cluster has its center within r_{180b} along the line of sight (this removes ~ 400 of the original ~ 23000 lines of sight). In addition, to allow fair inter-comparisons, only lines of sight which have reliable mass measurements for all methods are included; the ~ 90 lines of sight with fewer than 8 galaxies making the cut for a velocity dispersion estimate, or either richness < 1.1 are also removed. These cuts will have some effect on the scatters we consider but would be expected to be identifiable observationally.

We take the logarithm of these observables and that of the true mass M to find the mean relations for all clusters with $M \geq 10^{14} h^{-1} M_\odot$. We find relations for bins of M vs. observables, because of the large scatter at low mass. The fits are done by throwing out 3σ outliers for three iterations. This gives us our map between the observables and mass estimates $M_{N_{\text{red}}}, M_{N_{\text{ph}}}, M_{\text{SZ}}, M_{\text{Vel}}, M_{\text{WL}}$.

The distribution of the fractional mass scatters, $(M_{\text{est}} - M_{\text{true}})/M_{\text{true}}$, for the five mass measurement methods along ~ 96 lines of sight for each of the 243 clusters, is shown in Fig. 1. The scatters range from ~ 0.2 - 0.5 , with the smallest mass scatters associated with Compton decrement⁸ and N_{ph} . Note that this work follows a theoretical approach where all the mass measurements are related to the known true mass, a quantity inaccessible in observations. In particular, the sample is cut on the unobservable value of M_{true} and the distributions we consider are $M_{\text{est}}(M_{\text{true}})$, not vice versa.⁹ For an observational sample based upon some measurement M_{est} , such as richness mass or weak lensing mass, often the quantity of interest is the scatter in $P(M_{\text{true}}|M_{\text{est}})$ (see also extended comments in §5).¹⁰

2.3 Filaments and Galaxy Subgroups

In section §4, cluster filament properties calculated in Noh & Cohn (2011) and cluster galaxy subgroup properties calculated in Cohn (2011) for this simulation are used. De-

⁸ Recall the caveats for both SZ and weak lensing measurements mentioned earlier, however.

⁹ We thank E. Rozo for extremely helpful discussions on this.

¹⁰ For example, the richness mass scatter in Fig. 1, looks essentially Gaussian, unlike the double peaked distribution found and studied in e.g. Cohn, Evrard, White et al. (2007); Erickson, Cunha & Evrard (2011). If looking at $P(M_{\text{true}}|M_{\text{est}})$, one will find clusters which are “blends”, i.e. several halos which contribute to one apparent halo, often with a higher M_{est} than any of the contributing halos. These blends (see also e.g. Gerke et al. (2005) for discussion) are the source of the bimodal mass distribution reported and used in these other papers.

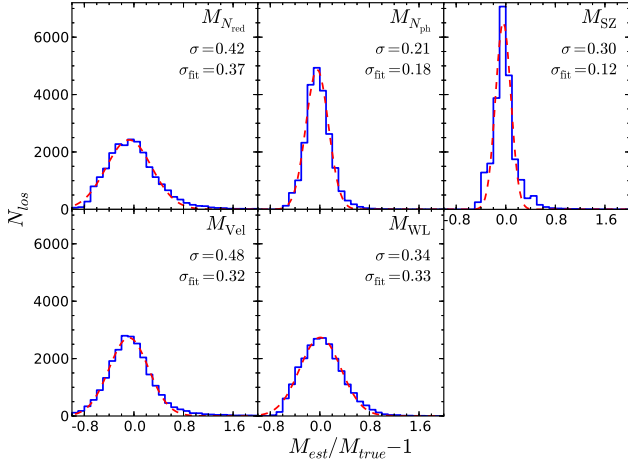


Figure 1. The fractional mass scatter, $M_{\text{est},i}/M_{\text{true}} - 1$ for all 243 clusters along ~ 96 lines of sight each, for the five mass measurement methods we consider. Solid lines are the masses estimated via N_{red} , N_{ph} , SZ (Compton decrement), velocity dispersion and WL (weak lensing) as described in section 2.2. An approximately 0.2-0.5 standard deviation is found. The (for the most part difficult to distinguish) dashed line is a least squares Gaussian fit, giving σ_{fit} , which is much smaller than the standard deviation for SZ. The WL and SZ mass scatter is expected to be strongly underestimated compared to true observations, as the 250 Mpc/h box size is too small to include all contributions to mass scatter along the line of sight to the observer, and in these two cases several known systematics are not included as well. See text for more information.

tailed background can be found in those two papers, but we briefly summarize some key aspects here.

Filaments are found in Noh & Cohn (2011) using a modification of the dark matter halo based filament finder of Zhang et al. (2009).¹¹ This filament finder searches for

¹¹ Although the cosmic web was noted years ago (Zel'dovich, Einasto & Shandarin 1982; Shandarin & Zel'dovich 1983; Einasto et al. 1984; Bond, Kofman & Pogosyan 1996), no unique filament finder exists. A variety of finders are in use, based on a wide range of dark matter, halo and/or galaxy properties, including for example Barrow, Bhavsar & Sonoda (1985); Mecke, Buchert & Wagner (1994); Sahni, Sathyaprakash & Shandarin (1998); Schmalzing et al. (1999); Colombi, Pogosyan & Souradeep (2000); Sheth et al. (2003); Colberg, Krughoff & Connolly (2005); Pimblet (2005a,b); Stoica et al. (2005); Novikov, Colombi & Dore (2006); Arag3n-Calvo et al. (2007a); Colberg (2007); Hahn et al. (2007a); van de Weygaert & Schaap (2007); Sousbie et al. (2008b); Stoica, Martinez & Saar (2007); Bond, Strauss & Cen (2010a); Forero-Romero et al. (2009); Gonzalez & Padilla (2010); Pogosyan et al. (2009); Sousbie, Colombi & Pichon (2009); Stoica, Martinez & Saar (2010); Wu, Batuski, & Khalil (2009); Zhang et al. (2009); Arag3n-Calvo, Shandarin & Szalay (2010); Arag3n-Calvo, van de Weygaert & Jones (2010); Bond, Strauss & Cen (2010b); Murphy, Eke & Frenk (2011); Sousbie (2011); Way, Gazis & Scargle (2011); Shandarin (2011); Shandarin, Habib & Heitmann (2011); Genovese et al. (2012); Smith et al. (2012); Jasche & Wandelt (2012).

bridges $10 h^{-1} \text{Mpc}$ or smaller between halos above $3 \times 10^{10} h^{-1} M_{\odot}$, starting with the most massive halos as potential bridge endpoints. Some clusters (16/243) end up within filaments because of the finder, such as less massive clusters located between two close ($< 10 h^{-1} \text{Mpc}$) massive clusters and clusters closer than $3 h^{-1} \text{Mpc}$ to a larger cluster. The rest of the clusters each lie at the center of a filament map extending out to $10 h^{-1} \text{Mpc}$. We found that filaments, halo mass (halos with mass $\geq 3 \times 10^{10} h^{-1} M_{\odot}$) and galaxy richness all tended to lie in a planar region around each cluster. We characterized these regions by taking a fiducial $3 h^{-1} \text{Mpc}$ high disk centered on the cluster which extends out to the edge of the radius $10 h^{-1} \text{Mpc}$ sphere. We use the planes related to halo and filament mass below. For halo mass, we randomly sampled 10,000 orientations to maximize the halo mass fraction in the plane (relative to the halo mass in the $10 h^{-1} \text{Mpc}$ sphere). For filaments, we considered planes spanned by the cluster and pairs of filament endpoints, and then took the plane which enclosed the most filament mass. This plane was not found for clusters lying within filaments. See Noh & Cohn (2011) for more details. We consider four quantities from this analysis below: $f_{M_{\text{hplane}}}$ (halo mass fraction in plane relative to that in $10 h^{-1} M_{\odot}$ sphere), $f_{M_{\text{fplane}}}$ (cluster filament mass fraction in plane relative to sphere), and the respective plane normal directions \hat{n}_{mass} , \hat{n}_{fil} .

Galaxy subgroups were characterized in Cohn (2011) for this simulation. These are groups of galaxies that fell into a cluster as part of a shared halo at an earlier time. Within the clusters, they share some coherence in space and time which can remain for several Gyr. We will use for each cluster its largest (richest) galaxy subgroup, in particular its fractional richness relative to that of the cluster, $f_{R_{\text{sub}}}$, its displacement relative to the cluster center, divided by the cluster long axis $f_{D_{\text{sub}}}$, and the directions of its position and average velocity relative to the cluster center, \hat{r}_{sub} , \hat{v}_{sub} .

2.4 Principal Component Analysis

For context and background, we summarize PCA and our notation here (see, e.g. Jolliffe (2002) for extensive discussion). PCA can be used when there are several correlated or covariant quantities. It is essentially a rotation of axes to find linearly independent bases (i.e. quantities which are not covariant or correlated), and is based on a model where some underlying average linear relation is present. We will apply PCA in a few different contexts.

Our starting application will be for individual clusters. For each individual cluster and line of sight, we have several different methods to estimate the true cluster mass. Each line of sight can thus be associated with five numbers, where each number is the mass measured in one method. These numbers can then be thought of as coordinates in some five dimensional abstract space, with each axis in this space corresponding to a different measurement method. All of the different lines of sight considered together then give a cloud of points in this space of measurement methods. PCA gives the properties of the “shape” of the mass scatters in this space, around their average values for the combined observations, for each cluster. We will consider these shapes and how they relate to other cluster prop-

erties. In addition, correspondences can be found between large mass scatters and physical properties or directions of the cluster. The PCA direction with smallest mass scatter is useful as well. Taking the ensemble of clusters, groups of properties which change together can be inferred by using PCA on the full set of correlations (this latter approach was pioneered by Jeason-Daniel et al. (2011); Skibba & Maccio (2011); Einasto et al. (2011)).

There are other uses of PCA, and caveats as well. PCA is often used to find the minimum set of variables needed to describe a system to some accuracy, for instance the dominant contributing basis vectors composing a galaxy spectrum. As far as caveats go, one concern is that if correlated variables are not scattered around a linear relation, a simple rotation of basis using PCA will not usefully separate them. For this reason, sometimes other functions are used besides the variables themselves, e.g. logarithms, when it is suspected that variables might be related by power laws.

For illustration, we take a set hypothetical measurements for two methods, as shown in Fig. 2. Each pair of measurements, by the two methods, is a position, i.e. a dot, in this plane labeled by two coordinates. We take one coordinate to be the shifted mass using red galaxy richness, $M_{N_{\text{red}}}^{\alpha} = M_{N_{\text{red},\text{est}}}^{\alpha} - \langle M_{N_{\text{red},\text{est}}}^{\alpha} \rangle$, and the other to be the shifted weak lensing mass, $M_{\text{WL}}^{\alpha} = M_{\text{WL},\text{est}}^{\alpha} - \langle M_{\text{WL},\text{est}}^{\alpha} \rangle$. Here, α denotes which particular point is being measured and the average is over all the points shown, all α values, i.e. $\langle M_{N_{\text{red},\text{est}}}^{\alpha} \rangle = \frac{1}{N_{\alpha}} \sum_{\alpha} M_{N_{\text{red},\text{est}}}^{\alpha}$. The vector $\vec{M}_{\text{obs}}^{\alpha}$ denotes $(M_{N_{\text{red}}}^{\alpha}, M_{\text{WL}}^{\alpha})$ and N_{α} is the number of measurements (points) indexed by α . For our first application below, all different values of α pertain to the same cluster, but label different lines of sight. The shift by the average over all the points (all α) guarantees that $\langle M_{\text{WL}} \rangle = \langle M_{N_{\text{red}}} \rangle = 0$.

Diagonalizing the covariance matrix for $(M_{N_{\text{red}}}, M_{\text{WL}})$, i.e. found by summing over all α , produces orthonormal eigenvectors $\hat{P}C_i$ (principal components) with eigenvalues λ_i . The eigenvectors are illustrated in Fig. 2 and are the axes of a new coordinate system in the space of measurement methods in which the measurements have zero covariance. The $\hat{P}C_i$ can be expressed in terms of the original basis directions,

$$\hat{P}C_i = \beta_{\text{red},i} \hat{e}_{\text{red}} + \beta_{\text{WL},i} \hat{e}_{\text{WL}}, \quad (1)$$

which identifies the mass scatters contributing most to each $\hat{P}C_i$. For example, if $\beta_{\text{red},0}$ is large, then most of the scatter in the direction of $\hat{P}C_0$ also lies in the direction of \hat{e}_{red} . One also sees how different scatters are related. In this simple example the biggest scatters come from increases or decreases in both $M_{\text{red}}, M_{\text{WL}}$ simultaneously. This implies, in this case, that $\hat{P}C_0$ might be related to an average overall mass shift, amongst methods, as well. Note that the overall signs for the $\hat{P}C_i$ are arbitrary.

A point (or vector from origin, labeled by α) in the original space can then be rewritten in the basis spanned by $\hat{P}C_0, \hat{P}C_1$:

$$\vec{M}^{\alpha} = M_{\text{red}}^{\alpha} \hat{e}_{\text{red}} + M_{\text{WL}}^{\alpha} \hat{e}_{\text{WL}} = a_0^{\alpha} \hat{P}C_0 + a_1^{\alpha} \hat{P}C_1. \quad (2)$$

For example, the point marked by a star in Fig. 2 has coordinates $\vec{M}^{\star} = 10^{14} \hat{e}_{\text{red}} + 10^{14} \hat{e}_{\text{WL}} = \sqrt{2} \times 10^{14} \hat{P}C_0 + 0 \hat{P}C_1$. That is, $(M_{\text{red}}^{\star}, M_{\text{WL}}^{\star}) = (1, 1) \times 10^{14}$ (assuming measurements are in units of $h^{-1} M_{\odot}$) and $(a_0^{\star}, a_1^{\star}) = (\sqrt{2}, 0) \times 10^{14}$.

The variances in each of the new directions, associated

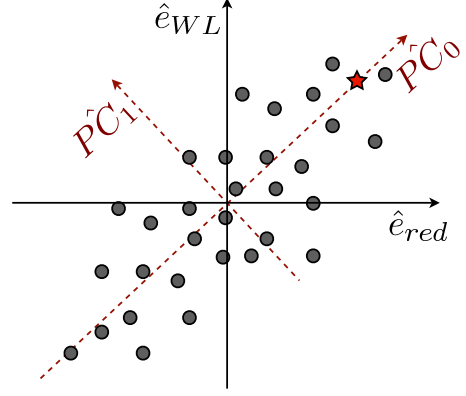


Figure 2. Principal component analysis takes a set of correlated measurements (using two methods shown as basis elements $\hat{e}_{\text{red}}, \hat{e}_{\text{WL}}$) and rotates their coordinates to a new basis, shown as dotted lines, where the measurements are uncorrelated. For example, the point marked as a star (i.e. $\alpha = \star$) is $\vec{M}^{\star} = 10^{14} \hat{e}_{\text{red}} + 10^{14} \hat{e}_{\text{WL}} = \sqrt{2} \times 10^{14} \hat{P}C_0 + 0 \hat{P}C_1$. The generalization to more measurement methods and thus a higher dimensional space is immediate. Amongst the orthonormal $\hat{P}C_i$, we choose $\hat{P}C_0$ to be along the direction of largest scatter (i.e. to correspond to the largest variance, λ_0), $\hat{P}C_1$ to be along the direction of second largest variance, etc., as described in the text.

with the coefficients a_i^{α} , are the eigenvalues of the principal components. Thus, λ_0 is the eigenvalue associated with $\hat{P}C_0$, etc. For all PCA eigensystems we consider here, we will order $i < j$ if $\lambda_i > \lambda_j$ and define $\sum \lambda = \sum_i \lambda_i$ and $\prod \lambda = \prod_i \lambda_i$. Generally, if there are N_{method} measurement methods, there are N_{method} $\hat{P}C_i$, spanning an N_{method} dimensional space. In Fig. 2, $N_{\text{method}}=2$; when we consider the five different mass measurement methods below, for example, $N_{\text{method}} = 5$. For PCA applied to different cluster properties, in §4.3 below, we have $N_{\text{method}} = 24$. We will apply PCA to covariance and correlation matrices, using the Pearson covariance $\text{Cov}(xy) = \frac{1}{N_{\alpha}-1} \sum_{\alpha=1}^{N_{\alpha}} (x_{\alpha} - \bar{x})(y_{\alpha} - \bar{y})$ where \bar{x} is the average of the N_{α} points x_{α} , etc., and $\text{Cov}(x, y) / \sqrt{\text{Cov}(x, x) \text{Cov}(y, y)}$ its associated correlation, for N_{α} measurements.¹²

The sum of the λ_i , $\sum \lambda$, is the sum of the variances of the measurement methods, their product, $\prod \lambda$, is related to the “volume” in this space of scatters, i.e. how the measurements are spread out in the space of measurement methods (specifically, for the example in Fig. 2, $\sqrt{\lambda_0 \lambda_1}$ is proportional to the area of the ellipse). A small eigenvalue λ_i means that the scatter in the corresponding $\hat{P}C_i$ direction is small, i.e. that the volume of scatters is roughly confined to a lower

¹² For the cluster mass scatters, as this covariance can be affected by outliers, we experimented with several outlier rejection schemes. As the resulting values were somewhat similar, and our analysis is in part just to provide an example, we use the untrimmed Pearson covariances and correlations hereon. We also considered for some properties (as did some of the earlier cluster PCA work) the Spearman correlation. The Spearman correlation coefficient uses the ranking of the measurements rather than the raw measurements themselves. Trends were similar to the Pearson covariances and correlations.

dimension. In particular, if most of the scatter is due to λ_0 , then there is a close to linear relation present. Such lower dimensionality was used in Einasto et al. (2011) to come up with scaling relations for superclusters. For PCA of correlations, a large λ_0 occurs if the initial measurements via different methods have strong correlations; for covariances, a large λ_0 can also occur if an individual measurement method has large scatter.

Measurement methods $M_{\text{obs},j}^\alpha$ (in the example $M_{N_{\text{red}}}, M_{\text{WL}}$) with the largest correlation or covariance with a_i^α (their projection on $\hat{P}C_i$) can be thought of as those dominating the scatter in the direction of $\hat{P}C_i$. This covariance or correlation is not unrelated to the measurement method's contribution to $\hat{P}C_i$, ($\beta_{\text{obs},j,i}$ in Eq. 1). The covariance or correlation is largest when $\beta_{\text{obs},j,i}$ is large, and when the eigenvalue λ_i is large relative to the other $\beta_{\text{obs},j}$'s and λ_i . (For PCA on correlations in particular, $\langle M_{\text{obs},j} a_i \rangle / \sqrt{\langle M_{\text{obs},j} M_{\text{obs},j} \rangle \langle a_i a_i \rangle} \sim \beta_{\text{obs},j,i} \lambda_i / \sqrt{\lambda_i \sum_k \lambda_k \beta_{\text{obs},j,k}^2}$; if $\lambda_0, \beta_{\text{obs},j,0}$ are large and a_0 is considered then this approaches 1.)

To summarize, PCA is a method taking a set of measurements via different methods which are correlated and separating them into uncorrelated combinations. In particular, if one denotes each set of measurements as a position in some space, along axes corresponding to each type of measurement method, then PCA is a rotation of coordinates in this space. The volume and shape traced out by the points representing the measurements are related to the PC eigenvectors and eigenvalues, and the direction in the space corresponding to the largest PC eigenvector is the combination of measurement methods with the largest scatter in its distribution.

3 VARIATIONS FOR A SINGLE CLUSTER DUE TO LINE OF SIGHT EFFECTS

As mentioned in the introduction, many of the mass measurement method scatters in Fig. 1 are comparable in size because they are due to similar properties of the cluster or its environment. Correlations between the scatters are thus expected, and as noted above, these correlations and their consequences become increasingly important as multiwavelength studies become more common.

We first consider each cluster and its line of sight mass scatters separately. In this way, the “true” object and its true mass remained fixed; all variations in scatters are due to changes in line of sight. Several examples of correlations for these scatters were already noted and illustrated in WCS¹³, and correlations with various physical properties (discussed below) were further studied in Noh & Cohn (2011); Cohn (2011). Here we statistically describe these correlations and covariances. We characterize cluster to cluster trends and variations in line of sight mass scatters and predicted masses, and then apply PCA to these scatters.

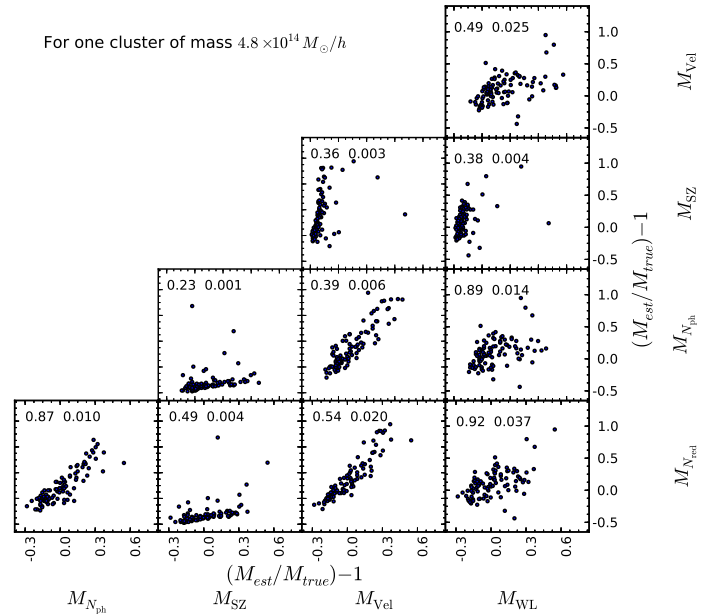


Figure 3. Cluster mass scatters ($M_{\text{est}}/M_{\text{true}} - 1$) for one cluster of mass $4.8 \times 10^{14} h^{-1} M_\odot$, along 95 lines of sight. The correlation and covariance for each mass measurement method pair is shown at the top of each panel (the y-axis is for a larger scale to allow room for these numbers). Large correlations are present for many pairs of mass measurement methods.

3.1 Correlated mass scatters for different cluster observables

To give an idea of the correlations and covariances for our five different mass measurement methods, we start with an example: the 10 pairs of mass measurements for a single cluster ($M = 4.8 \times 10^{14} h^{-1} M_\odot$) shown in Fig. 3. Each panel shows a different pair of mass estimates along all lines of sight (i.e. $N_\alpha = 95$), and correlations and covariances are listed at the top of each. We use $M_{\text{est}}/M_{\text{true}} - 1$ to focus on fractional mass scatter. As can be seen, many of the correlations are large.

For all 243 clusters, the correlations for the same pairs of mass measurement methods are compiled in Fig. 4, with medians and averages given in Table 1. Strong correlations are frequent. For each cluster, at least one pair of mass measurement methods has correlation > 0.4 , and the largest pair correlation is often larger, ~ 0.7 . Within our cluster sample, the mass scatters for $(M_{N_{\text{red}}}, M_{N_{\text{ph}}})$ are most often the highest correlated pair. The other measurement method pairs which frequently have the highest correlation (but not as often as $(M_{N_{\text{red}}}, M_{N_{\text{ph}}})$) are $(M_{N_{\text{red}}}, M_{\text{SZ}})$, $(M_{N_{\text{red}}}, M_{\text{WL}})$, $(M_{N_{\text{ph}}}, M_{\text{SZ}})$ and $(M_{N_{\text{ph}}}, M_{\text{WL}})$. The pair with the minimum correlation is most frequently $(M_{\text{Vel}}, M_{\text{WL}})$ (closely followed by $(M_{\text{Vel}}, M_{\text{SZ}})$, and $(M_{\text{Vel}}, M_{N_{\text{ph}}})$).

For our PCA analysis below, we will use covariances instead, shown in Fig. 5, with medians and averages given in Table 1. These are more relevant for understanding the actual mass scatters and how they change together, rather than, for example, how much a relatively large M_{SZ} mass scatter corresponds to a relatively large $M_{N_{\text{red}}}$ mass scatter. As the fractional mass fluctuations (the σ values in Fig. 1)

¹³ An example of correlations between velocity dispersion and weak lensing measurements are shown in WCS Fig. 14

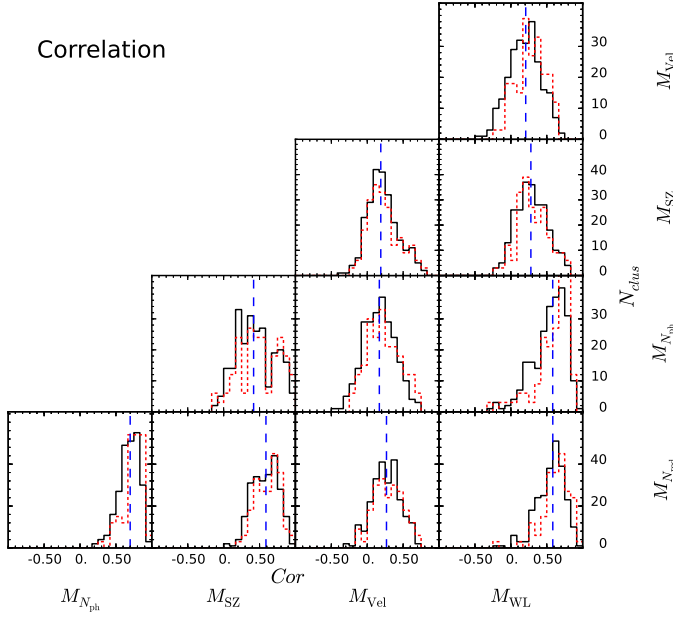


Figure 4. Correlations of $M_{\text{est}}/M_{\text{true}} - 1$ for pairs of mass measurement methods ($M_{N_{\text{red}}}$, $M_{N_{\text{ph}}}$, M_{SZ} , M_{Vel} , M_{WL}). The solid line is the distribution of cluster mass scatter correlations, for all clusters individually, for the same pairs as in Fig. 3. The dotted line corresponds to the 70 clusters with mass $\geq 2 \times 10^{14} h^{-1} M_{\odot}$. The vertical dashed lines are at the median values which are listed in Table 1, along with the average values. Note that the x-axis, the range of correlations, has a scale which varies widely between different types of measurement method pairs.

Pair	Ave Cor	Med Cor	Ave Cov	Med Cov
$M_{N_{\text{red}}} - M_{N_{\text{ph}}}$	0.68	0.70	0.025	0.017
$M_{N_{\text{red}}} - M_{\text{SZ}}$	0.58	0.59	0.037	0.017
$M_{N_{\text{red}}} - M_{\text{Vel}}$	0.26	0.27	0.031	0.023
$M_{N_{\text{red}}} - M_{\text{WL}}$	0.55	0.58	0.031	0.028
$M_{N_{\text{ph}}} - M_{\text{SZ}}$	0.44	0.42	0.012	0.005
$M_{N_{\text{ph}}} - M_{\text{Vel}}$	0.17	0.17	0.007	0.006
$M_{N_{\text{ph}}} - M_{\text{WL}}$	0.53	0.58	0.013	0.011
$M_{\text{SZ}} - M_{\text{Vel}}$	0.22	0.19	0.018	0.008
$M_{\text{SZ}} - M_{\text{WL}}$	0.29	0.28	0.008	0.006
$M_{\text{Vel}} - M_{\text{WL}}$	0.19	0.21	0.016	0.013
$M_{N_{\text{red}}} - M_{N_{\text{red}}}$	–	–	0.084	0.062
$M_{N_{\text{ph}}} - M_{N_{\text{ph}}}$	–	–	0.015	0.012
$M_{\text{SZ}} - M_{\text{SZ}}$	–	–	0.070	0.014
$M_{\text{Vel}} - M_{\text{Vel}}$	–	–	0.205	0.142
$M_{\text{WL}} - M_{\text{WL}}$	–	–	0.045	0.041

Table 1. Average and median values for the distribution (for 243 clusters) of pairs of mass measurement method correlations shown in Fig. 4 and covariances shown Fig. 5.

tend to be about 0.3, the covariance sizes should be compared to ~ 0.09 . The largest covariances are between ($M_{N_{\text{red}}}$, M_{WL} and M_{Vel}). Each cluster has at least one covariance ≥ 0.01 . In contrast, the minimum covariance between measurement methods tends to be between the pair ($M_{N_{\text{ph}}}$, M_{SZ}).¹⁴

¹⁴ If the abovementioned neglected weak lensing and SZ scatter is uncorrelated with local properties of the cluster, as expected,

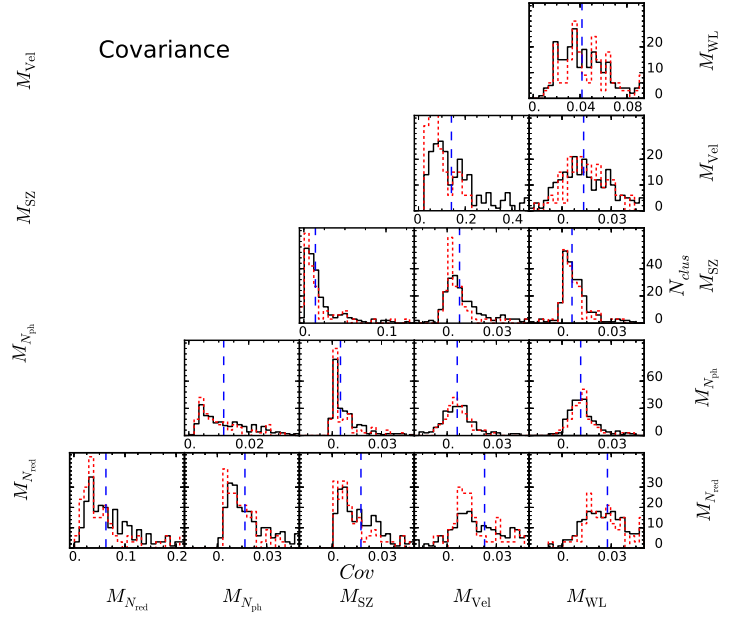


Figure 5. Covariances of $M_{\text{est}}/M_{\text{true}} - 1$ for pairs of mass measurement methods ($M_{N_{\text{red}}}$, $M_{N_{\text{ph}}}$, M_{SZ} , M_{Vel} , M_{WL}). The solid line shows the distribution of cluster mass scatter covariances, for all clusters individually, and the same mass observation pairs as in Figs. 3,4. The dotted line restricts to the 70 clusters with mass $\geq 2 \times 10^{14} h^{-1} M_{\odot}$. As the characteristic mass scatter for most clusters is about 0.3, the range for covariances shown is ± 0.05 . The vertical dashed lines are at the median values, which are also listed in Table 1. Note that the x-axis, the range of covariances, has a scale which varies with types of mass measurement method pairs.

Some of these correlation and covariance trends are understandable (larger covariances tend to go with quantities with larger scatter more generally and vice versa), but others rely upon the interplay between different measurement methods and the causes of the scatter. The relative importance of different contributions to these were not a priori obvious to us, although reasons could be found for trends. For instance, the two richnesses often are the most correlated mass measurement pair. This is perhaps because both use the same objects (galaxy counts), so that an enhancement or decrement of $M_{N_{\text{ph}}}$ (galaxies making the spectroscopic cut) might be more likely accompanied by a similar change in $M_{N_{\text{red}}}$ (galaxies making the red sequence cut), than by changes in the mass measurements by other methods. Other mass measurement methods are correlated with richness less directly (for M_{SZ} and M_{WL} the measurements and thus presumably the scatter are more directly tied to the dark matter distribution rather than the biased galaxies; M_{Vel} just seems to be weakly correlated with most things). In section §3.3 we compare the PCA results (scatters which

when this scatter is included the majority of the covariances will not change (except possibly the one between weak lensing and SZ, as they can possibly have correlated changes in their scatter due to structure outside the box). However, the correlations will change as they are divided by the correlations of SZ with itself or weak lensing with itself.

occur together) with physical cluster directions to get some idea of which properties might be driving covariant mass measurement method scatters.

3.2 PCA for individual clusters

We now apply PCA to the covariances for $\vec{M}_{\text{obs}}/M_{\text{true}}$ for each individual cluster, to get a new basis,

$$\frac{\vec{M}_{\text{obs}}}{M_{\text{true}}} = \frac{\vec{M}_{\text{est}}^\alpha}{M_{\text{true}}} - \frac{\vec{M}_{\text{ave}}}{M_{\text{true}}} = \sum_i a_i^\alpha \hat{P}C_{i,M}. \quad (3)$$

The subtracted offset $\vec{M}_{\text{ave}} \equiv \langle \vec{M}_{\text{est}} \rangle$, where the average is over all the lines of sight for each cluster of interest, i.e., there is a different \vec{M}_{ave} for each cluster. The median (and rms around zero) values for the ensemble of clusters, for $|\vec{M}_{\text{ave}}/M_{\text{true}} - 1|$ are [0.21 (0.32), 0.11 (0.17), 0.08 (0.15), 0.11 (0.18), 0.18 (0.27)] for $M_{N_{\text{red}}}, M_{N_{\text{ph}}}, M_{\text{SZ}}, M_{\text{Vel}}, M_{\text{WL}}$ respectively. The relative sizes of the line of sight scatters around the average mass, $\vec{M}_{\text{obs}}/M_{\text{true}} - \vec{M}_{\text{ave}}/M_{\text{true}}$ compared to the line of sight averaged mass around the true mass $\vec{M}_{\text{ave}}/M_{\text{true}} - 1$ varies widely cluster to cluster. Except for velocity dispersions, the rms scatters of $(\vec{M}_{\text{obs}}/M_{\text{true}} - \vec{M}_{\text{ave}}/M_{\text{true}})$ is $\geq |\vec{M}_{\text{ave}}/M_{\text{true}} - 1|$ for 50-60 percent of the clusters and the median value of $|\vec{M}_{\text{obs}}/M_{\text{true}} - \vec{M}_{\text{ave}}/M_{\text{true}}|$ is $\geq |\vec{M}_{\text{ave}}/M_{\text{true}} - 1|$ for about 30-40 percent of the clusters, for velocity dispersions the numbers are closer to 90 and 70 percent respectively.

As in section §2.4, and by the definition in Eq. 3, M_{obs} refers to mass measurements which have zero average when summed over the sample of interest. Any vector in this space can of course be written in terms of the orthonormal basis $\hat{P}C_{i,M}$; what is special for \vec{M}_{obs} is that the variances of the a_i^α are equal to λ_i for gaussian scatter. Because there are five mass scatters, there are five PC vectors $\hat{P}C_{i,M}$ per cluster, with eigenvalues $\lambda_{i,M}$, again ordered $\lambda_{0,M} > \lambda_{1,M} > \lambda_{2,M}$ and so on. We use the subscript M to distinguish these PC vectors from others which will be considered in section 5, and take $M_{\text{obs},i}$, with $i = 0, 1, 2, 3, 4$, to correspond to $(M_{N_{\text{red}}}, M_{N_{\text{ph}}}, M_{\text{SZ}}, M_{\text{Vel}}, M_{\text{WL}})$ and similarly for $\hat{e}_{\text{obs},i}$. We also have, as in Eq. 1,

$$\hat{P}C_{i,M} = \sum_{\text{obs},j=0}^4 \beta_{\text{obs},j,i} \hat{e}_{\text{obs},j}. \quad (4)$$

We first consider the PC eigenvalues, the $\lambda_{i,M}$. There are some trends: the fractional scatter in the largest direction ($\frac{\lambda_{0,M}}{\sum \lambda} \sim 0.7$), but can vary from 0.4 to ~ 1 , as shown in Fig. 6. The relatively large contribution from $\lambda_{0,M}$ means that the variance is strongly dominated by the single combination of mass scatters in the direction of $\hat{P}C_{0,M}$. As seen in Fig. 6, bottom, $\lambda_{0,M}, \lambda_{1,M}, \lambda_{2,M}$ together comprise almost all the variance for most clusters. The presence of some mass measurement methods with small scatter suggests that there are some directions of the combined measurement methods which would also have small scatter and thus small $\lambda_{i,M}$, and this is seen in the much smaller values of $\lambda_{4,M}$ and sometimes $\lambda_{3,M}$. The distribution of covariance matrices shown in Fig. 5 determine the $\lambda_{i,M}$ when combined with the relation of the covariances to each other, cluster by cluster. The combination of measurement methods in $\hat{P}C_{4,M}$ which has the smallest variance, $\lambda_{4,M}$ in our case, is also interesting, we return to this in §5.

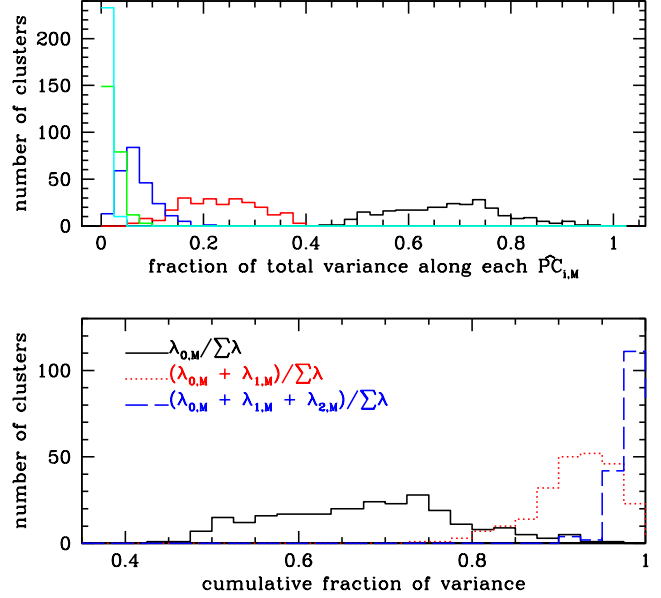


Figure 6. (Top) Peaks from right to left: fraction of covariance (i.e. scatter) $\frac{\lambda_{0,M}}{\sum \lambda}, \frac{\lambda_{1,M}}{\sum \lambda}, \frac{\lambda_{2,M}}{\sum \lambda}$, etc. On average $\frac{\lambda_{0,M}}{\sum \lambda} \sim 0.7$. (Bottom) Peaks from left to right: fraction of covariance from scatter in direction of $\hat{P}C_{0,M}, \hat{P}C_{0,M}$ or $\hat{P}C_{1,M}$, etc. Most of the scatter is in the directions spanned by $\hat{P}C_{0,M}, \hat{P}C_{1,M}, \hat{P}C_{2,M}$, with a substantial fraction in the direction of the largest scatter.

The sum and product of the $\lambda_{i,M}$ for all clusters are shown on a logarithmic plot in Fig. 7. The sum of scatters can vary by a factor of ~ 30 from cluster to cluster, and tends to be dominated by $\lambda_{0,M}$, while the product of the $\lambda_{i,M}$ can be made very small (its size varies by over 10^7) if some directions, especially $\hat{P}C_{4,M}$, have very little scatter. In §4 below, these scalar properties of the cluster mass scatter will be compared to physical cluster properties such as triaxiality and mass.

Turning to the PC vectors, many clusters have similar $\hat{P}C_{0,M}$ (i.e. the combination of mass scatters that dominates is similar for many of the clusters). To quantify this more generally, we took $\hat{P}C_{i,M,\text{minsq}}$ as the direction which minimizes $(\hat{P}C_{i,M} \cdot \hat{P}C_{i,M,\text{minsq}})^2$ for the full ensemble of 243 clusters ($\hat{P}C_{0,M,\text{minsq}}$ is shown in the first line of Table 2). Fewer than 20 percent of the clusters have their $\hat{P}C_{0,M}$ pointing more than 45° away from $\hat{P}C_{0,M,\text{minsq}}$; about 25 percent have their $\hat{P}C_{1,M}$ pointing more than 45° away from $\hat{P}C_{1,M,\text{minsq}}$. We found that for almost all the clusters the projection upon $\hat{P}C_{1,M,\text{minsq}}$ is close in size to the projection on $\hat{P}C_{0,M,\text{minsq}}$, (i.e. 0.62 correlation). Continuing to $\hat{P}C_{4,M}$, the direction of least scatter, ~ 70 percent of the clusters are within 45° of $\hat{P}C_{4,M,\text{minsq}}$ given in Table 2. This minimum scatter direction is (not surprisingly) dominated by the $\hat{e}_{N_{\text{ph}}}, \hat{e}_{\text{SZ}}$ directions, since these are the mass measurement methods with the smallest scatter in our sample.¹⁵ The similar forms of the $\hat{P}C_i$ suggest that the mass

¹⁵ Again recall these particular coefficients do not carry over di-

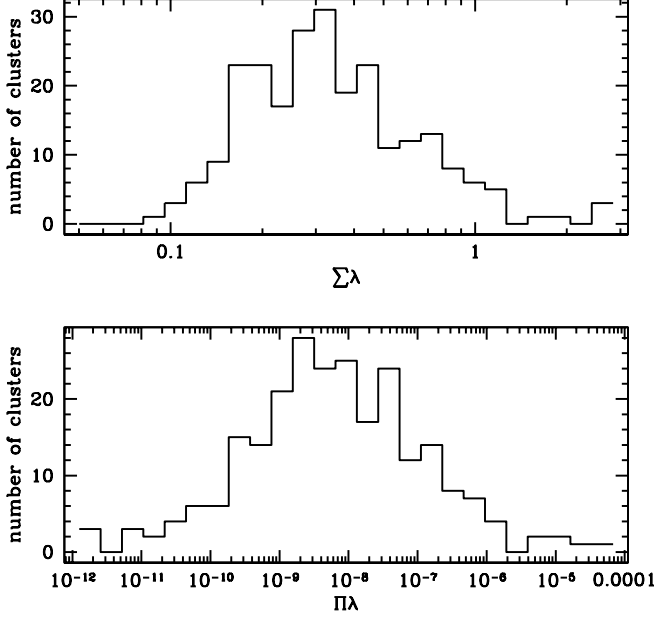


Figure 7. Sum and product of covariances for all clusters: the sum is dominated by the eigenvalue in the direction of largest scatter, $\lambda_{0,M}$, while the product, related to the volume in the space of scatters, can be made very small by small values of e.g. $\lambda_{4,M}$. The sum of eigenvalues peaks at ~ 0.3 , the product peaks around 10^{-8} .

scatter combinations they correspond to might have similar physical origins. For 75 percent of the clusters, the coefficients of $\hat{P}C_{0,M}$ are also all the same sign, that is that the dominant combination of scatter also has all the scatters increasing together relative to their average values, but 16/243 have large (< -0.1) opposite sign coefficients for some mass measurement methods. As a large fraction of the variance is captured by $\hat{P}C_{0,M}$, as seen in the large values of $\lambda_{0,M}/\sum\lambda$, the coefficient of $\hat{P}C_{0,M}$ for the any given line of sight is indicative of the size of scatter from the average along that line of sight.

The correlations of the five mass measurement methods $M_{\text{obs},i}$ with the $\hat{P}C_j$ coefficients a_j^α , for all clusters, are shown in Fig. 8. For the ensemble of cluster measurements, the largest correlation with a_0^α , i.e. with the coefficient of $\hat{P}C_{0,M}$, is for velocity dispersions (in part because most of the scatter is due to velocity dispersions). Correlations of a_0^α with the other mass measurement methods are relatively smaller, and of similar size to each other. Taking instead the fraction of the mass scatter vector due to $\hat{P}C_0$, i.e., $a_0^\alpha/\sqrt{\sum_i (a_i^\alpha)^2}$, the correlations are weaker. In addition, weaker correlations arise with the coefficients of $\hat{P}C_{1,M}$, and for the direction with the smallest direction of scatter, $\hat{P}C_{4,M}$, only $M_{N_{\text{ph}}}$ has a noticeable correlation on average.

The direction of $\hat{P}C_{0,M}$ can also be compared to that of $\vec{M}_{\text{ave}}/M_{\text{true}}$: the average inner product ~ 0.7 , but the peak

rectly to observations, most importantly because they are based on scatter in $P(M_{\text{est}}|M_{\text{true}})$ and not vice versa.

Directions	$\hat{e}_{N_{\text{red}}}$	$\hat{e}_{N_{\text{ph}}}$	\hat{e}_{SZ}	\hat{e}_{vel}	\hat{e}_{WL}
$\hat{P}C_0$					
$\hat{P}C_{0,M,\text{minsq}}$	0.42	0.14	0.19	0.83	0.29
$\hat{P}C_{0,M,\text{total}}$	0.52	0.21	0.31	0.69	0.34
$\hat{P}C_{0,M,\text{total,massive}}$	0.54	0.25	0.38	0.51	0.49
$\hat{P}C_4$					
$\hat{P}C_{4,M,\text{minsq}}$	0.15	-0.96	0.2	-0.01	0.15
$\hat{P}C_{4,M,\text{total}}$	0.32	-0.94	-0.02	0.006	0.098
$\hat{P}C_{4,M,\text{total,massive}}$	0.34	-0.94	0.03	0.02	0.06

Table 2. A comparison between different characteristic directions in the space of mass scatters, ($\hat{e}_{N_{\text{red}}}$, $\hat{e}_{N_{\text{ph}}}$, \hat{e}_{SZ} , \hat{e}_{vel} , \hat{e}_{WL}). The direction which minimizes the dot product squared with $\hat{P}C_{i,M}$ of all 243 clusters is $\hat{P}C_{i,M,\text{minsq}}$. $\hat{P}C_{i,M,\text{total}}$ are the vectors found by PCA analysis of all observed cluster masses (normalized by M_{true}) and all lines of sight, jointly, discussed in §5; $\hat{P}C_{i,M,\text{total,massive}}$ restricts to the 70 clusters with $M \geq 2 \times 10^{14} h^{-1} M_\odot$. These vectors are derived from our estimates of $M_{\text{est}}(M_{\text{true}})$, which as mentioned earlier, neglects some systematics for WL and SZ and relies upon our simulation calibrated mass definitions in terms of observables.

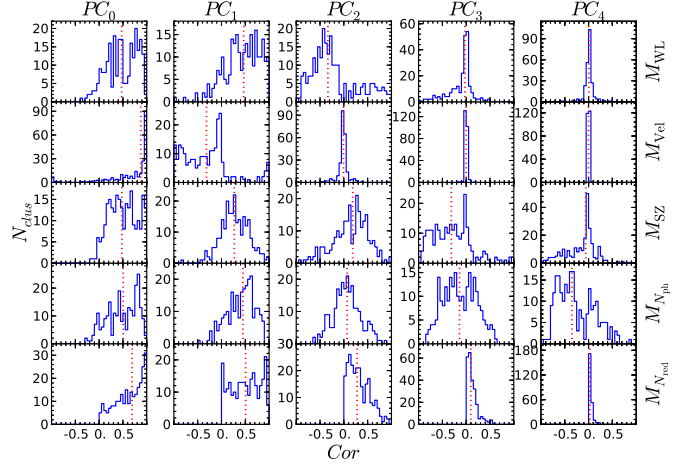


Figure 8. The correlations between the observed mass scatters and their projected values on $\hat{P}C_{i,M}$. Velocity dispersions are very strongly correlated with the direction of the largest scatter, $\hat{P}C_{0,M}$ in part because the component of $\hat{P}C_{0,M}$ in the velocity dispersion direction, $\beta_{\text{vel},0}$, tends to be large. The dotted line marks the median value of the correlations. Note that the y-axis scale varies with mass measurement method and $\hat{P}C_i$, the x-axis does not.

is closer to 0.8, and there is a broad range of values. (The rest of the vector $\vec{M}_{\text{ave}}/M_{\text{true}}$ seems to lie in the $\hat{P}C_{1,M}, \hat{P}C_{2,M}$ plane). That is, the direction of largest mass measured is close to that of largest scatter; presumably this is because this direction has large scatters generally.

We now compare the above quantities to line of sight dependent cluster properties. We will follow this in section §4 with properties depending on the entire cluster rather than a given line of sight.

3.3 Relation to cluster line of sight properties

To get more understanding of the PCA decomposition, we compare values of PC quantities along lines of sight to clus-

ter properties along those lines of sight. The PCA line of sight dependent properties we consider are the coefficients a_i^α of the $\hat{P}C_{i,M}$, $a_i^\alpha / \sqrt{\sum_j (a_j^\alpha)^2}$ (the fraction of scatter in different $\hat{P}C_i$ directions, i and j each run from 0 to 4), and the total scatter for a given line of sight ($\sum_i (a_i^\alpha)^2 / \lambda_{i,M}$). We correlate these with the angle θ_{obs} between the line of sight and six specific physical cluster directions, listed below.

Previously, for this simulated data set, increased mass scatter was found by observing along certain physical cluster directions by WCS; Noh & Cohn (2011); Cohn (2011). Our extension using PCA includes six physical directions: the long axis $\hat{\ell}$ of the cluster, calculated using the dark matter particles in the simulation with a FoF finder as mentioned above, the plane normal containing the most halo mass \hat{n}_{mass} , or connected filament mass \hat{n}_{fil} centered on the cluster (see §2.3 and Noh & Cohn (2011) for more details), the direction of the largest subgroup of galaxies \hat{r}_{sub} which originated from the same infall host halo (see §2.3), and the velocity direction \hat{v}_{sub} of this largest subgroup.¹⁶ Many of these special cluster directions are similar to each other, e.g. Kasun & Evrard (2005); White, Cohn & Smit (2010); Cohn (2011), as expected.

The correlation of $a_i^\alpha / \sqrt{\sum_j (a_j^\alpha)^2}$ (the fraction of the mass scatter in the $\hat{P}C_{i,M}$ direction, for the line of sight indexed by α) with $|\cos \theta_{\text{obs}}|$ for each observation is shown in Fig. 9. The medians and the averages of these correlation coefficient distributions are shown in Table 3. The largest average correlations of angles with the physical cluster axes are with $\hat{P}C_{0,M}$, the direction of the combination of mass scatters that dominates the scatter. The average correlations with $\hat{P}C_{1,M}$ are slightly smaller, for the rest of the $\hat{P}C_{i,M}$ the average correlations tend to zero (as can be seen, the individual clusters can have larger correlations). For $\hat{P}C_{0,M}$, the largest correlation is with the direction of the cluster long axis $\hat{\ell}$. The next largest signals are with the direction of the mass plane normal \hat{n}_{mass} , filament plane normal \hat{n}_{fil} , and the direction of the largest substructure \hat{r}_{sub} . The velocity of the largest substructure \hat{v}_{sub} and the direction of the most massive filament \hat{r}_{fil} are more weakly correlated. That is, scatter dominated by the mass scatter combination in $\hat{P}C_{0,M}$ tends to occur more often when the direction of observation is more aligned with the long axis of the cluster. (As the other cluster directions are not linearly independent, strong correlations with them are possible and seen as well.) As most of the scatter occurs along $\hat{P}C_{0,M}$ and $\hat{P}C_{1,M}$, both of which are most correlated with looking along the long axis, it suggests that most of the scatter is due to looking along the long axis $\hat{\ell}$.

The correlation with a_0^α , the full contribution from $\hat{P}C_{0,M}$, rather than the fractional contribution above, was much weaker.

One other line of sight quantity, $\sum_i (a_i^\alpha)^2 / \lambda_{i,M}$ (the weighted scatter of M_{obs}^α), also tends to have correlations

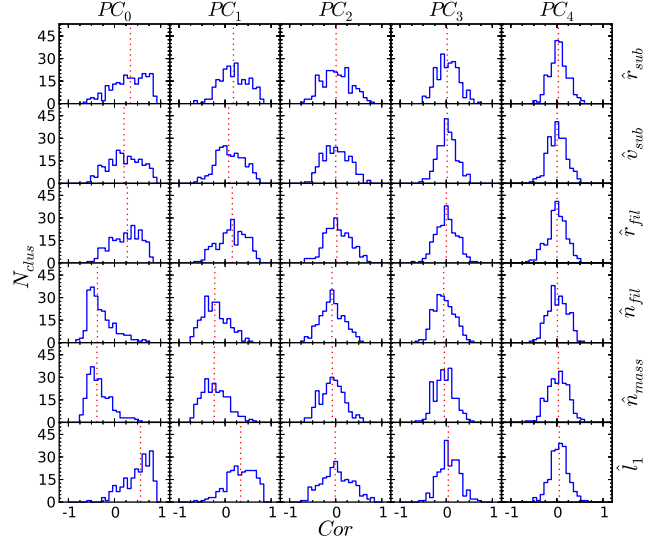


Figure 9. Correlations between the fraction of the line of sight mass scatter in the $\hat{P}C_{0,M}$ direction and $|\cos \theta_{\text{obs}}|$. The cluster physical directions are $\hat{\ell}$, the long axis of the cluster, \hat{n}_{mass} , the direction perpendicular to the mass disk with radius $10 h^{-1} \text{Mpc}$ and width $3 h^{-1} \text{Mpc}$ centered on the cluster, containing the majority of the mass in halos, \hat{n}_{fil} , similar to \hat{n}_{mass} in shape and volume, but oriented to contain the majority of the filamentary mass ending on the cluster, \hat{r}_{fil} , the direction to the most massive halo filament surrounding the cluster, and $\hat{v}_{\text{sub}}, \hat{r}_{\text{sub}}$, the relative velocity and direction of the largest galaxy subgroup in the cluster. See text and §2.3 for more detailed definitions. Only the 227 clusters which are filament endpoints are included in the comparisons concerning filament planes. Vertical dotted lines denote medians, and the averages and medians are shown in Table 3. The largest contributions to $\hat{P}C_0$, for most clusters, seem to come when observing along the long axis of the cluster, but there is a wide scatter. The correlations with the mass and filament planes are maximized for observations along the planes, i.e. perpendicular to the normal vectors $\hat{n}_{\text{mass}}, \hat{n}_{\text{fil}}$, as expected.

with special cluster directions as seen in Fig. 10. The largest fraction of clusters with correlations > 0.20 occurs with the long axis.¹⁷

To summarize this section, each cluster’s line of sight mass scatter variations and correlations were analyzed and

¹⁶ We also measured correlations with another direction dependent quantity, the amount of substructure found via the Dressler-Schechter (Dressler & Schechter 1988) test, as described in White, Cohn & Smit (2010); Cohn (2011); however, the correlations with $\hat{P}C_{0,M}$ were much weaker with this directional dependent quantity than with the ones reported here.

¹⁷ Correlations with the cluster long axis and external filaments or nearby clusters, both possible causes of mass scatters, have been seen in many other works too, e.g. van de Weygaert & Bertschinger (1996); Splinter et al. (1997); Colberg et al. (1999); Chambers, Melott & Miller (2000); Onuora & Thomas (2000); Faltenbacher et al. (2002); van de Weygaert (2002); Hopkins, Bahcall & Bode (2004); Bailin & Steinmetz (2005); Faltenbacher et al. (2005); Kasun & Evrard (2005); Basilakos et al. (2006); Lee & Evrard (2007); Lee et al. (2008); Paz, Stasyszyn & Padilla (2008); Pereira, Bryan & Gill (2008); Ragone-Figueroa & Plionis (2007); Costa-Duarte, Sodre, & Durret (2011); Ceccarelli et al. (2011); Paz et al. (2011), correlations with the long axis and mass scatters specifically have been discussed recently in, e.g., Becker & Kravtsov (2011); Marrone et al. (2012); Battaglia, Bond, Pfrommer & Sievers (2011); Bahe, McCarthy & King (2012); Feroz & Hobson (2012).

	$\hat{PC}_{0,M}$	$\hat{PC}_{1,M}$	$\hat{PC}_{2,M}$	$\hat{PC}_{3,M}$	$\hat{PC}_{4,M}$
\hat{r}_{sub}	0.35(0.31)	0.18(0.19)	0.01(0.02)	0.02(0.03)	0.03(0.04)
\hat{v}_{sub}	0.21(0.22)	0.08(0.10)	0.00(0.01)	0.02(0.02)	0.01(0.01)
\hat{r}_{fil}	0.28(0.24)	0.16(0.15)	0.03(0.04)	0.00(0.01)	0.00(0.00)
\hat{n}_{fil}	-0.37(-0.29)	-0.22(-0.21)	-0.08(-0.08)	-0.06(-0.04)	0.01(0.02)
\hat{n}_{mass}	-0.38(-0.32)	-0.24(-0.21)	-0.07(-0.07)	-0.04(-0.04)	0.03(0.02)
\hat{l}_1	0.56(0.50)	0.34(0.33)	-0.01(0.02)	0.04(0.06)	0.05(0.05)

Table 3. The median of correlation coefficients between the fraction of the line of sight mass scatter covariance in each $\hat{PC}_{i,M}$ direction and $|\cos \theta_{obs}|$. The average is shown in the parenthesis. The full distribution is shown in Fig. 9.

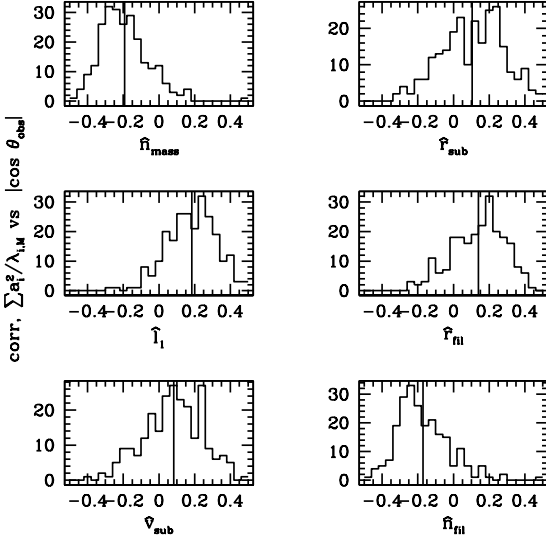


Figure 10. Correlations of $\sum_i (a_i^\alpha)^2 / \lambda_{i,M}$ (the weighted scatter of M_{obs}^α) with angle between line of sight and various cluster axes, as described in the text and in Fig. 9. Vertical lines are at average value.

characterized separately using PCA. Both similarities (similar large scatter directions) and differences (raw size of scatter, amount of variation with line of sight) were found. The scatter was usually dominated (large $\lambda_{0,M} / \sum \lambda$) by one combination of mass scatters, which also tended to become an increasing component of the total mass scatter as the angle of observation became more aligned along the cluster's long axis.

4 CLUSTER TO CLUSTER VARIATIONS

Now we turn to line-of-sight independent properties, PCA related or otherwise. The scatters of each cluster are also characterized by several numbers, i.e. scalars, which are not dependent upon the line of sight of observation (e.g. λ_0). Here we take some characteristic mass scatter scalars for each cluster and compare them with other cluster properties, intrinsic to the cluster or due to its environment, combining to give 24 quantities in total. We make use of several quantities obtained previously (WCS; Noh & Cohn (2011); Cohn (2011)) for this simulation and described in §2.3. We use correlations rather than covariances, to take out the dimensional dependence. After considering properties of the

pairwise correlations in §4.2, we consider the full ensemble of correlations using PCA in §4.3.

4.1 Cluster quantities

For each cluster we consider the following (note that mass scatters are for $\vec{M}_{obs} = \vec{M}_{est} - \langle \vec{M}_{est} \rangle = \vec{M}_{est} - \vec{M}_{ave}$):

- $\Delta M_i \equiv (M_{ave,i} - M_{true}) / M_{true}$, observed average mass offsets for each of the five observables considered earlier: red galaxy richness, phase richness, SZ, velocity dispersions and weak lensing respectively. Note that these correlations are identical to those of $M_{ave,i} / M_{true}$.
- $|\cos \theta_{0,mins q}|$, i.e. $|\hat{PC}_{0,M} \cdot \hat{PC}_{0,M,mins q}|$, the angle between the largest mass scatter direction for each cluster, $\hat{PC}_{0,M}$, and the direction $\hat{PC}_{0,M,mins q}$, given in Table 2, which minimizes the dot product with $\hat{PC}_{0,M}$ for all the clusters.
- $\sum \lambda$, the sum of the cluster's mass scatters in §3.2.
- $\prod \lambda$, the product of the cluster's scatters in §3.2.
- $\frac{\lambda_{0,M}}{\sum \lambda}$ fraction of total (mass scatter) variance along direction of largest variance in §3.2.
- $\lambda_{1,M}$, variance along the direction with second largest mass scatter variance in §3.2.
- $\lambda_{4,M}$, variance along the direction with smallest mass scatter variance in §3.2.
- $T = \frac{l_1^2 - l_2^2}{l_1^2 - l_3^2}$, triaxiality, where the l_1, l_2, l_3 are the axes of cluster, calculated using the dark matter particles in the FoF halo.
- $S = \frac{l_3}{l_1}$ ($l_1 > l_2 > l_3$), sphericity.
- $f_{M_{plane}}$, the fractional connected filamentary mass in the local plane around clusters defined in §2.3.
- $f_{M_{hplane}}$, the fractional halo mass in the local plane around clusters, see §2.3.
- M_{sphere} , the mass in halos above $5 \times 10^{13} h^{-1} M_\odot$ within a $10 h^{-1} Mpc$ radius sphere of the cluster. We used the sum of large halo masses in a $10 h^{-1} Mpc$ radius sphere around the central cluster rather than the total mass because the former is already known to be correlated with the mass of the central halo (e.g., Noh & Cohn (2011)).
- M_{true} , the cluster (FoF $b = 0.168$) mass (also called M).
- $f_{R_{sub}}$, the fractional richness of the largest galaxy subgroup (see §2.3).
- $f_{D_{sub}}$, the ratio of the distance to the largest galaxy subgroup in the cluster to the length of the longest cluster axis (see §2.3).
- c_{vir} , the concentration (not scatter from mean concentration of a given mass), from fitting all of the Friends of Friends halo particles to an NFW (Navarro, Frenk & White 1997) profile. This was found to be very important in the previous studies (Jeeson-Daniel et al. 2011;

Skibba & Maccio 2011; Einasto et al. 2011) inspiring this work.

- $t_{1:3}$, the time of most recent $\geq 1:3$ merger (often taken as the threshold for a merger-driven starburst)
- $t_{1:10}$, the time of most recent $\geq 1:10$ merger (often taken as a threshold for merger-driven AGN feeding)
- x_{off} , the distance between the central galaxy position and the average of the galaxy positions. This is similar to the “relaxedness” considered by Skibba & Maccio (2011), but in that case they use the offset between the most bound particle and the halo center of mass. We also considered scaling by $M^{1/3}$, the results did not change significantly.
- $\cos \theta_{\Delta,0}$, the cosine of the angle between \vec{PC}_0 and \vec{M}_{ave} , i.e., the largest mass scatter direction vs. the average mass offset direction.

We thus have a space of dimension $N_{\text{method}} = 24$ for the correlation and PCA analysis below. Several of these quantities might be expected to be related. For instance, sphericity and triaxiality both characterize departures from perfect spheres, but triaxiality measures prolateness and oblateness while sphericity is sensitive to flatness. Similarly the sum and product of the eigenvalues probe the size of the largest eigenvalue and in principle how the largest and smallest eigenvalue change together, respectively. A priori, it isn’t clear which of our large set of quantities have the strongest or most illuminating relations to each other, so we start with a large set.

4.2 Correlations

Fig. 11 summarizes the pairwise correlations. For simplicity, only correlations which have absolute value > 0.2 , in six ranges, $\pm 0.2, \pm 0.35, \pm 0.5$, are shown. The correlations of measurements with themselves are omitted. Filled dark (open red) symbols are positive (negative) correlations. Properties in the list are grouped by type: offsets of cluster average mass measurements from their true mass (“ ΔM ”, defined in §4.1), PCA related scalars for each cluster from §3.2 (“ λ_M ”), cluster environment or shape (“phys1”), cluster history (“phys2”), and $|\cos \theta_{\Delta,0}|$. Relations between measurements of the same sort (e.g. concentration and time of last merger, etc.) can be seen in the diagonal boxes.

The off-diagonal boxes thus correlate different sorts of cluster properties. We concentrate on these. The first thing to notice is that many large correlations are visible. We start with correlations with $\Delta \vec{M}$, each cluster’s five average fractional mass measurement offsets, corresponding to the five measurement methods. The different components of $\Delta \vec{M}$ often have similar correlations with other quantities. In particular, they are all strongly correlated with sphericity, most are anticorrelated with triaxiality and all are anticorrelated with the offset of the average galaxy position. All but the weak lensing mass offset are also correlated with the smallest mass variance $\lambda_{4,M}$, that is, when the average mass offsets ΔM_i are large, the variance in the direction of minimum scatter around the average measured value tends to be large as well: the line of sight averaged scatter often is increasing for clusters with larger mass scatters around these averages. There is also a trend of these average mass offsets being anticorrelated with signatures of relaxedness (fractional richness

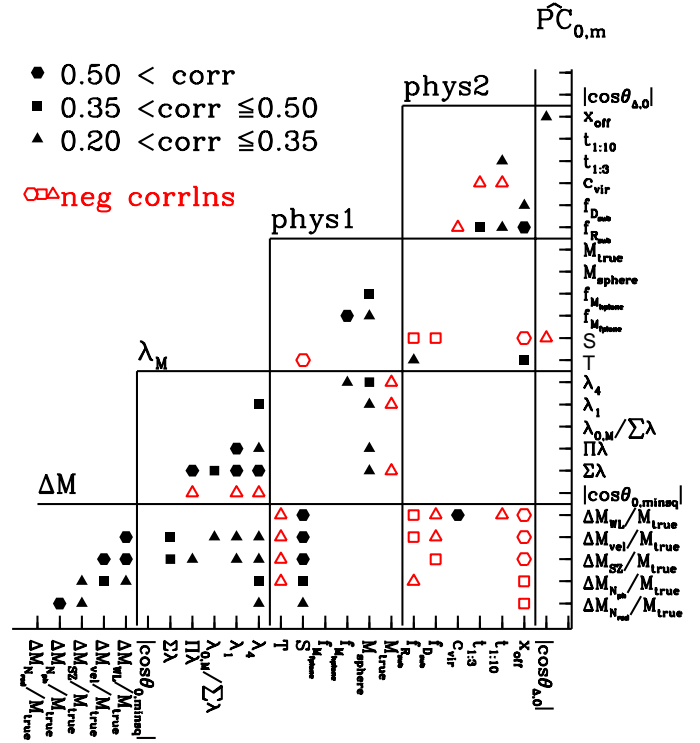


Figure 11. Correlations between cluster properties: $0.5 < \text{corr}$ (filled hexagons), $0.35 < \text{corr} \leq 0.5$ (filled squares), $0.2 < \text{corr} \leq 0.35$ (filled triangles), opposite signs are open versions of the same symbols, i.e. $\text{corr} < -0.5$ (open hexagon), etc. Auto-correlations are not shown. Cluster properties are described in section 4.1. A blank space means that a correlation has absolute value ≤ 0.2 . The horizontal and vertical lines distinguish the types of cluster properties. ΔM labels the five components of $\Delta \vec{M}$. λ_M refers to measurements for that cluster’s mass scatter correlations. “phys1” refers to cluster properties which are environmental or shape related. “phys2” refers to cluster properties more related to substructure or merging (concentration, distance to largest substructure, etc.), λ_0 refers to dot product or correlation with $\vec{PC}_{0,M}$. Only half of the correlations are shown, as they are symmetric across the diagonal axis.

of the largest subgroup, offset of the average galaxy position relative to the galaxy center, etc.).

Turning to other correlations with the mass scatter variances, an increase in the mass in halos around the cluster tends to be accompanied by an increase many of the measures of mass scatter, i.e. properties associated with the $\lambda_{i,M}$. This might indicate the presence of a supercluster. The size of the smallest mass scatter variance $\lambda_{4,M}$ also seems to increase with increasing fractional halo mass in the plane of the cluster, $f_{M_{\text{plane}}}$.

Lastly, triaxiality is correlated with indicators of substructure, (the offset of the galaxy average position from the central galaxy and the fractional richness of the largest galaxy subgroup), while in contrast sphericity is anticorrelated with these, as well with the fractional distance of the

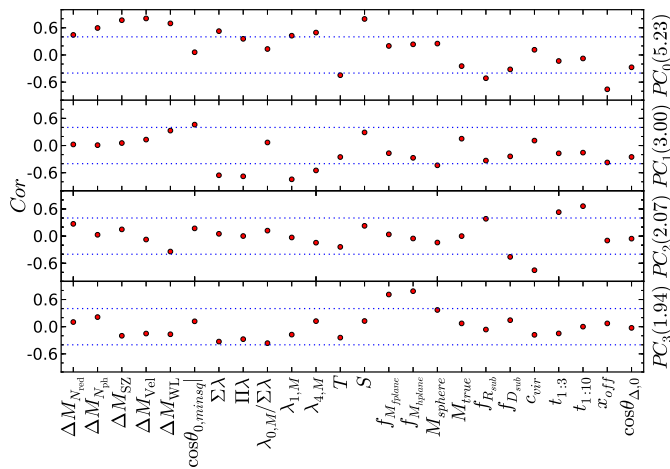


Figure 12. Correlation coefficients between the cluster properties listed in §4.1 and their projection on the first four principal components. Horizontal dotted lines at ± 0.4 are to guide the eye to larger positive or negative correlations. The top box is for \hat{PC}_0 , the second is for \hat{PC}_1 and so on; the expansion of the \hat{PC}_i vectors is given by these correlations divided by the λ_i eigenvalues, 5.23, 3.0, 2.07, 1.94 respectively for $\hat{PC}_0, \hat{PC}_1, \hat{PC}_2, \hat{PC}_3$.

largest galaxy subgroup from the cluster center. Physically, one might expect a rich subgroup in the cluster to lie along the long axis of the cluster (e.g. coming from a filament feeding matter into the cluster) and be correlated with a lengthened (more triaxial) cluster as a result.

4.3 PCA

By using PCA on these pairwise correlations, more general groupings can be investigated. This application of PCA to our sample is an extension of PCA of several cluster properties studied by Jeesson-Daniel et al. (2011); Skibba & Maccio (2011) and by Einasto et al. (2011) for superclusters, which inspired this study. Properties correlated by Jeesson-Daniel et al. (2011); Skibba & Maccio (2011) included virial mass, concentration, age, relaxedness, sphericity, triaxiality, substructure, spin, and environment. Jeesson-Daniel et al. (2011) used 1867 halos from several boxes with masses ranging from $\sim 10^{11} h^{-1} M_\odot$ up and found that the dominant PC vector was most correlated with halo concentration. Skibba & Maccio (2011) used several boxes with halos with masses $\geq 10^{10} h^{-1} M_\odot$, and also found halo concentration to be important for clusters, as well as halo mass and degree of relaxedness.¹⁸ Our sample is closest to the high mass tail of these samples.

¹⁸ For superclusters in SDSS DR7, Einasto et al. (2011) considered weighted luminosity, volume, diameter, density of the highest density peak of galaxies and the number of galaxies, as well as shape parameters, and used the two largest \hat{PC}_i to find scaling relations. They divided up the sample into two sets of superclusters based upon where they lay in the planes spanned by pairs of $\hat{PC}_0, \hat{PC}_1, \hat{PC}_2$.

The 24 PC eigenvalues¹⁹ are $\lambda_i / \sum \lambda = (0.22, 0.12, 0.09, 0.08, 0.07, 0.05$ (3 times), $0.04, 0.03$ (4 times), 0.02 (3 times), 0.01 (6 times), < 0.005 (2 times)). Unlike the case of mass scatter, where $\lambda_{0,M}$ is relatively large, (on average $\lambda_{1,M}/\lambda_{0,M} < 0.4$), here $\lambda_1/\lambda_0 \sim 0.6$, and $(\lambda_1, \lambda_2, \lambda_3, \lambda_4) = (5.23, 3.00, 2.07, 1.95)$, fairly close to each other. This makes interpretation less straightforward. However, subsets of properties with strong correlations with individual \hat{PC}_i may indicate these properties change together. To better identify relations, one can take these subsets and do PCA on the correlations within this subset alone. An example is given below. The expansion coefficients of the \hat{PC}_i for the different measured quantities, the β_i in Eq. 1, are given by the correlations divided by the eigenvalues. (For example, the expansion coefficients of the \hat{PC}_0 in the order listed in §4.1 are $(0.19, 0.26, 0.34, 0.35, 0.30, 0.03, 0.23, 0.16, 0.06, 0.19, 0.22, -0.20, 0.35, 0.09, 0.10, 0.11, -0.11, -0.22, -0.14, 0.05, -0.06, -0.03, -0.33, -0.12)$.)

The strongest correlation is between the velocity dispersion mass offset ΔM_{Vel} and \hat{PC}_0 (~ 0.8), 9 other properties have correlations with absolute value above or equal to 0.7 with at least one of the \hat{PC}_i ($i \leq 6$). Considering smaller correlations, 21/24 of the properties have at least one correlation of absolute value ≥ 0.5 with one of the \hat{PC}_i , $i \leq 11$, and all properties have at least one correlation ≥ 0.4 with at least one \hat{PC}_i . The correlations of the first four principal component vectors with the 24 properties are shown in Fig. 12. Lines are drawn at ± 0.4 to guide the eye to the larger correlations. The sign of the correlations with the eigenvectors depends upon the overall sign of the eigenvectors, which is arbitrary, but the relative signs of the correlations of the different properties with each eigenvector are not arbitrary.

We begin with \hat{PC}_0 , the direction of largest variation. The ΔM_i 's, the sum of the mass scatter variances $\sum \lambda$, the individual mass scatter variances $\lambda_{1,M}, \lambda_{4,M}$ and sphericity S all have large correlations (≥ 0.4) with their projections onto \hat{PC}_0 . These correlations are in the opposite sense of those of $T, f_{R_{\text{sub}}}$ and x_{off} (these latter three might indicate less relaxed halos). A relation between large triaxiality and an increased offset in the average galaxy position or the presence a rich subgroup is somewhat intuitive, but the sign of the relation to the average mass measured for the cluster is surprising. One interpretation of the relation between ΔM_i and T seen both here and in the correlations is that clusters which are more triaxial have fewer lines of sight along the elongated and presumably large measured mass direction, so that fewer lines of sight result in a large $\bar{M}_{\text{est}}/\bar{M}_{\text{true}} - 1$. See also related discussion in Rasia et al. (2012).²⁰

To go further, we considered the subset of properties which correlate strongly with \hat{PC}_0 ($\Delta M_i, S, T, f_{R_{\text{sub}}}, x_{\text{off}}, \sum \lambda, \lambda_{1,M}, \lambda_{4,M}$) and applied PCA to their intercorrelations. The trends with \hat{PC}_0 for these quantities appear with the direction $\hat{PC}_{0,\text{subset}}$ as well. In this case,

¹⁹ Some of the previous analyses consider logarithms of the scalar quantities, we redid the analysis taking logarithms of $\sum \lambda, \prod \lambda, \lambda_{1,M}, \lambda_{4,M}, f_{M_{\text{plane}}}, f_{M_{\text{hplane}}}, f_{R_{\text{sub}}}, f_{D_{\text{sub}}}, c, M_{\text{sphere}}, M$ and found very similar results for correlations with the first 2 \hat{PC}_i as below, for \hat{PC}_2 , correlations roughly increased for the merger related quantities, and decreased for the M_{sphere} and plane environment quantities.

²⁰ We thank E. Rasia for discussions about this.

however, $\lambda_{0,\text{subset}}$ is relatively larger, $\lambda_{0,\text{subset}}/\sum\lambda = 0.39$. To help in understanding, we took three groups of properties (1) ΔM_i (except ΔM_{WL}); (2) the mass scatter measures $\sum\lambda, \lambda_{1,M}, \lambda_{4,M}$; and (3) $T, f_{R_{\text{sub}}, x_{\text{off}}}, S, \Delta M_{\text{WL}}$. The properties in (1) and (2) have large same sign correlations with \hat{PC}_0 . For (3), sphericity S and average weak lensing mass offset ΔM_{WL} have this sign correlation as well, while $T, f_{R_{\text{sub}}, x_{\text{off}}}$ have the opposite sign. These three groups (roughly) can be seen in correlations with $\hat{PC}_{1,\text{subset}}$ (0.17 of the sum of eigenvalues), but in this case the relative behavior between properties in (2) and (3) reverses (i.e. increased mass scatter now has the opposite correlation with \hat{PC}_1 as increased sphericity does), and changes in (1) all have correlations < 0.07 with $\hat{PC}_{1,\text{subset}}$. (Note that the general orthogonality of the \hat{PC}_i means relations between properties, i.e. relative sizes and signs of correlations, do have to change from one \hat{PC}_i vector to another.) The correlation strengths change as well, going from \hat{PC}_0 to \hat{PC}_1 , increasing for (2) and decreasing (below 0.4) for (3). Considering the trends in broad brush, for a given cluster, large measured average (over lines of sight) mass offsets from true mass, aside from weak lensing, seem to tend to come with high sphericity and large mass measurement scatters, and low triaxiality, $f_{R_{\text{sub}}, x_{\text{off}}}$. That is, when a cluster's mass offsets are very large, there is a tendency for the vector of all its properties to be lying far along $\hat{PC}_{0,\text{subset}}$, implying trends for the other properties. When average mass offsets (besides ΔM_{WL}) are small, it is not clear whether a given cluster's variations are lying along $\hat{PC}_{0,\text{subset}}$ or $\hat{PC}_{1,\text{subset}}$ or some other direction. As the relation between large sphericity (and small triaxiality, $f_{R_{\text{sub}}, x_{\text{off}}}$), i.e., (3), and the size of mass measurement scatters, i.e., (2), reverses between these two PCA vectors, small mass offsets makes it difficult to estimate the relation between them (i.e., between (2) and (3)).

Continuing with the full set of 24 properties, and considering correlations with \hat{PC}_1 , the large sphericity/small triaxiality, (relatively) small richness in biggest subgroup, (relatively) small distance of largest subgroup from center and small offset of average galaxy positions with central galaxy position relation trends are also seen, but more weakly. Fluctuations in the direction of \hat{PC}_1 have an increase in $|\hat{PC}_{0,M} \cdot \hat{PC}_{0,M,\text{minsq}}|$ tied to a decrease in overall mass scatter ($\sum\lambda, \prod\lambda, \lambda_{1,M}, \lambda_{4,M}$) and a decrease in mass in nearby large halos M_{sphere} . This last perhaps indicates that the alignment of $\hat{PC}_{0,M}$ is better, and the mass scatter smaller, when the cluster is not in a supercluster. Low concentration and relative distance of the largest subgroup from the cluster center are accompanied by earlier major mergers for variations in the direction of \hat{PC}_2 . The fraction of mass in the filament and mass planes seem to change together for changes along \hat{PC}_3 , along with the amount of mass in nearby large halos. Again, these last 3 properties can be studied alone via PCA. In this case the associated $\lambda_{0,\text{subset}}/\sum\lambda = 0.65$. Note this is a different subset of PC vectors than considered earlier, and corresponds to all three quantities, normalized by covariance, changing by about the same amount with the same sign. This may imply that clusters which are in a richer environment, that is, with more nearby halos, may have the mass around them distributed in a more planar shape.

We experimented with a larger set of properties than

shown here, including for example the quantities shown in the first column of Fig. 9 for each cluster, i.e. the correlations with projections on $\hat{PC}_{0,M}$ and physical directions. In this case the correlations with \hat{PC}_0 for the other quantities remained essentially as shown in the top line of Fig. 12 but the $\hat{PC}_{0,M}$ -long axis projections and the $\hat{PC}_{0,M}$ -direction of largest subgroup projections had large correlations with \hat{PC}_0 in the same sense as T , cluster triaxiality.

5 AN ENSEMBLE OF CLUSTERS

The previous sections considered cluster directional mass scatters and variations in properties, cluster to cluster. One can also consider the joint ensemble of mass measurements of all the simulated clusters and all their lines of sight, for all five methods. A comparison is interesting between the PC vectors of the individual clusters, for many lines of sight, and those for all the clusters together.

5.1 Trends for all clusters considered together

We take the union of the estimated masses of all clusters and all lines of sight (aside from those discarded as discussed in §2) and repeat the analysis of §3. Now $\vec{M}_{\text{obs}}/M_{\text{true}} = \vec{M}_{\text{est}}/M_{\text{true}} - \langle \vec{M}_{\text{est}}/M_{\text{true}} \rangle$. The average $\langle \vec{M}_{\text{est}}/M_{\text{true}} \rangle$ is over all clusters and lines of sight, and for our case is within a few percent of 1. The resulting covariance matrix for these mass scatters is shown in Table 4. The covariances for the combined sample are larger than the averages for individual clusters, the latter are shown in Table 4 in parentheses for comparison, and were plotted individually in Fig. 5. The increased scatter is not unexpected as it is a combination of scatters from objects which are all themselves scattered around different central values. The corresponding PC eigenvalues are $\lambda_{i,M,\text{total}} = (0.31, 0.18, 0.094, 0.061, 0.022)$. The direction of largest scatter has $\lambda_{0,M,\text{total}}/\sum\lambda \sim 0.47$, compared to the average of 0.66 for individual clusters shown in Fig. 6. The total mass scatter variance $\sum\lambda = 0.67$, which is relatively high compared to the average for individual clusters; the product $\prod\lambda$ is also relatively larger (7×10^{-6}), as to be expected from the increased covariances in Table 4.²¹ The directions of largest scatters are similar to those for the clusters considered separately (Table 2), although $\hat{PC}_{4,M,\text{total}}$ has a much smaller SZ component than $\hat{PC}_{4,M,\text{minsq}}$. The correlations with $\hat{PC}_{0,M,\text{total}}$ of the projections of the different mass observables ($M_{N_{\text{red}}}, M_{N_{\text{ph}}}, M_{\text{SZ}}, M_{\text{Vel}}, M_{\text{WL}}$) are (0.69, 0.57, 0.57, 0.79, 0.57), similar to the median of their individual cluster counterparts, (0.69, 0.51, 0.48, 0.87, 0.47), shown in Fig. 8. The correlations are fairly large for the other \hat{PC}_i components, but these by definition contribute less to the total mass scatter. $\hat{PC}_{0,M,\text{total}}$ and $\Delta\vec{M}$ are 23° apart, similar to their counterparts for the individual clusters. Again, just as for individual clusters, the closer one is to the long axis of the cluster, the larger the

²¹ For the 70 clusters with mass $\geq 2 \times 10^{14} h^{-1} M_\odot$, the total scatter $\sum\lambda$ goes down (to 0.44 from 0.67 for the sample with $M \geq 10^{14} h^{-1} M_\odot$), and the direction of the $\hat{PC}_{0,M,\text{total}}$ slightly rotates as seen in Table 2. The fraction of variance in $\lambda_{0,M}$ increases, i.e. the direction of the largest scatter has more of the scatter.

	$M_{N_{\text{red}}}/M_{\text{true}}$	$M_{N_{\text{ph}}}/M_{\text{true}}$	$M_{\text{SZ}}/M_{\text{true}}$	$M_{\text{Vel}}/M_{\text{true}}$	$M_{\text{WL}}/M_{\text{true}}$
$M_{N_{\text{red}}}/M_{\text{true}}$	0.18 (0.08)	0.06 (0.02)	0.05 (0.04)	0.04 (0.03)	0.04 (0.03)
$M_{N_{\text{ph}}}/M_{\text{true}}$	0.06 (0.02)	0.04 (0.02)	0.02 (0.01)	0.02 (0.01)	0.02 (0.01)
$M_{\text{SZ}}/M_{\text{true}}$	0.05 (0.04)	0.02 (0.01)	0.09 (0.07)	0.04 (0.02)	0.04 (0.01)
$M_{\text{Vel}}/M_{\text{true}}$	0.04 (0.03)	0.02 (0.01)	0.04 (0.02)	0.24 (0.20)	0.05 (0.02)
$M_{\text{WL}}/M_{\text{true}}$	0.04 (0.03)	0.02 (0.01)	0.04 (0.01)	0.05 (0.02)	0.11 (0.05)

Table 4. Covariance matrix for full set of measurements $\vec{M}_{\text{obs}}/M_{\text{true}}$, for all clusters, and, in parentheses, the average of the individual cluster covariances in Fig. 4. The median values for the the individual cluster covariances tend to be smaller than the average values. The covariances for the full sample tend to be larger than the averages cluster to cluster.

fraction of scatter due to $\hat{P}C_{0,M,\text{total}}$ (~ 0.4 correlated, see, e.g. Fig. 9 for the individual cluster distribution). The next leading correlations of $\hat{P}C_{0,M,\text{total}}$ are with the position of the largest subgroup and the direction perpendicular to the cluster’s dominant filamentary plane or mass plane. These trends were very close to those found for clusters individually. These relations are still however based on the estimated mass as a function of true mass, and thus not immediately applicable to observational samples, as we now discuss.

5.2 Future extensions to observational samples

One can also consider using some variant of our PCA analysis for an observational sample, which would have some range of true cluster masses and some observations, as we do in our box. However, our implementation of PCA doesn’t directly carry over, and our measurement sample in hand is not appropriate. We discuss these limitations and possible ways forward here.

Observations are concerned with M_{true} as a function of estimated mass, $M_{\text{true}}(M_{\text{est}})$. An observer does not have M_{true} . We have instead been calculating $M_{\text{est}}(M_{\text{true}})$ and in addition dividing by M_{true} . Applying PCA in a way useful to observations (so that one can take 5 methods to measure mass of one cluster and compare to the PC vectors calculated in simulation) requires PC vectors calculated, from simulation, for a representative range of M_{est} and M_{true} , and a proxy for the unobservable M_{true} .²² As a proxy for M_{true} , one possibility is the likelihood mass. This would come from simulations, which are already required to calibrate covariances and offsets. Another possible mass proxy uses the principal component vectors directly, in principle encoding similar information. That is, one has from the definition of PC vectors,

$$\frac{\vec{M}_{\text{obs}}^\alpha}{M_{\text{true}}} = \frac{\vec{M}_{\text{est}}^\alpha}{M_{\text{true}}} - \left\langle \frac{\vec{M}_{\text{est}}}{M_{\text{true}}} \right\rangle = \sum_i a_i^\alpha \hat{P}C_{i,M}. \quad (5)$$

The quantities aside from M_{true} are either measured, e.g., $\vec{M}_{\text{est}}^\alpha$, or calculated from simulations, e.g., $\langle \vec{M}_{\text{est}}/M_{\text{true}} \rangle$, $\hat{P}C_{i,M}$. In particular, we have

$$\hat{P}C_{4,M,\text{total}} \cdot \left(\frac{\vec{M}_{\text{est}}^\alpha}{M_{\text{true}}} - \left\langle \frac{\vec{M}_{\text{est}}}{M_{\text{true}}} \right\rangle \right) = a_4^\alpha \quad (6)$$

²² Using no proxy for M_{true} , i.e. doing PCA on M_{est} alone, differently weights the scatter of high and low mass clusters. In our sample, caveats below, most of the scatter then corresponds to all mass estimates increasing or decreasing together in equal amounts. Projections on this combination of mass scatters are weakly correlated with observations along the long axis of the cluster, and less correlated with other directions.

but the variance of a_4 is given by $\lambda_{4,M,\text{total}}$. If $\lambda_{4,M,\text{total}}$ is very small then we can try the approximation $a_4 \sim 0$, so that projecting on $\hat{P}C_{4,M,\text{total}}$ gives the approximation²³

$$M_4 \sim \frac{\hat{P}C_{4,M,\text{total}} \cdot \vec{M}_{\text{est}}^\alpha}{\hat{P}C_{4,M,\text{total}} \cdot \left\langle \frac{\vec{M}_{\text{est}}}{M_{\text{true}}} \right\rangle}. \quad (7)$$

The general use of this approach depends upon the size of $\lambda_{4,M,\text{total}}$ for the system; the smaller $\lambda_{4,M,\text{total}}$ is, the better it appears this approximation should work. As there tend to be some minus signs in $\hat{P}C_4$, some catastrophic failures will occur where $M_4 \ll M_{\text{est},i}$, for all i .

However, the relevance of testing these possible M_{true} proxies on our sample seems limited. In particular, the $P(M_{\text{est}}|M_{\text{true}})$ for our sample (all $M \geq 10^{14} h^{-1} M_\odot$ halos observed along ~ 96 lines of sight each) is not representative of any expected observed sample, nor is our $P(M_{\text{true}})$, which is required for likelihoods. Observing our few high mass clusters along many lines of sight is not a good approximation to observing many clusters along one line of sight: the few high mass clusters observed along many lines of sight in particular do not well sample the realistic population of high mass clusters. There are no clusters appearing fewer than ~ 96 times; in particular, rare high mass clusters which would be expected from the number of lower mass clusters “present” are missing. Halos with the same M_{est} (the only observable) but a lower M_{true} will also occur in an observational sample, and might contribute differently to the scatter as well. It would also be important to include the neglected, in our simulation, line of sight larger scale scatter for SZ and weak lensing and the systematics mentioned above. These would be very interesting directions to pursue in future work.

In summary, in this section we considered all the clusters in the box, along all lines of sight, to see how cluster-to-cluster variation altered mass scatter relations found in earlier sections for individual clusters; the trends remained but changed in strength. In particular, the dominant mass scatter combination, similar in form to that for many of the individual clusters, still seems to be more prevalent when looking down the long axis of the cluster or perpendicular to the mass or filament plane of the cluster. In the second subsection, we mentioned two possible methods for extending our analysis which do not require prior knowledge of

²³ An extreme and unphysical limit of this case would be if one measurement method had tiny scatter and no correlation with the other measurement methods. In this case $\hat{P}C_{4,M,\text{total}}$ would be proportional to a measurement via this one method, and the last equation would basically give that the estimated mass in this method is the true mass; up to any overall biases that might exist, an unbiased mass estimator would make the denominator 1.

M_{true} , replacing it with the likelihood mass or a mass derived from $\hat{P}C_4$. These would be interesting to apply to an observational sample, but would need a very closely matched simulation. It would be interesting to see if the resulting PC vectors and projections on them by estimated mass measurement methods have correlations with cluster orientation or perhaps $M_{\text{proxy}}/M_{\text{true}}$.

6 OUTLIERS

We have focussed on general trends above, but not all clusters (or all lines of sight) fell on the general trends. We searched for properties of outliers or tails in the distributions of the various quantities related to $\lambda_{i,M}$, outliers in average cluster measured mass vs. true cluster mass, clusters with different maximum or minimum covariance mass measurement method pairs than the majority of clusters, and clusters where $\hat{P}C_{0,M}$ had at least one opposite sign coefficient with absolute value ≥ 0.1 (i.e. largest direction of scatter not corresponding to all mass scatters increasing together, mentioned earlier).

The various outliers did not seem to follow any pattern. Some outliers were common to a cluster, e.g. sometimes a large $\lambda_{4,M}$ outlier occurred with a large $\prod \lambda$, as might be expected, as $\lambda_{4,M}$ is the smallest of the $\lambda_{i,M}$. Some of the clusters which had $\hat{P}C_{0,M}$ not aligned with the most likely $\hat{P}C_{0,M,\text{minsq}}$ had much larger contributions to mass scatter from Compton decrement than the average cluster, often due to close massive halos, and $\lambda_{0,M}/\sum \lambda$ tending to be smaller than for the usual cluster. The clusters having different correlations of lines-of-sight properties with mass measurement methods don't seem to have a clear relation to the outliers in mass scatter properties.

7 SUMMARY AND DISCUSSION

The scatters between estimated and true cluster masses, for different observational methods, are often correlated. Understanding these correlations is becoming more and more important as reliance on multiwavelength measurements increases. For instance, correlations and covariances in scatters affect both error estimates in multiple measurements of individual clusters and produce a bias in measurements of stacked objects (see Rykoff et al. (2008); Stanek et al. (2010); White, Cohn & Smit (2010); Angulo et al. (2012) for detailed discussion). (Using the full covariance matrices has been done in some cluster analyses, e.g. by Rozo et al. (2009); Mantz et al. (2010); Benson et al. (2011).) We characterized the scatter and correlations of clusters in two ways.

We started by considering clusters individually to identify mass scatter properties due to line of sight effects for 243 clusters in an N-body simulation, each along ~ 96 lines of sight. We used five observational mass proxies: red galaxy richness, phase space galaxy richness, Sunyaev-Zel'dovich flux, velocity dispersions and weak lensing. It would also be very interesting to include X-ray observation as well, but our attempt at a proxy, based on assigning fractional X-ray flux to cluster galaxy subgroups, was not illuminating. These are employed to find cluster masses in current and upcoming large scale cluster surveys.

For each cluster, we characterized the “shape” and “volume” of the mass scatters of M_{est} calculated as a function of M_{true} , using PCA, or Principal Component Analysis, to obtain a set of non-covariant measurements. Most clusters had one combination of observational mass scatters contributing the majority of the mass scatter, and this combination was similar for many of the clusters, i.e. they had a similar largest principal component $\hat{P}C_{0,M}$. This scatter combination was a larger fraction of the total line of sight mass scatter when the cluster was observed along the long axis of the cluster. Weaker relations with observations along other cluster intrinsic and environmental axes were seen. Identifying the long axis of course requires the clusters to have non-spherical shapes. In our case the cluster member dark matter particles were determined using the FoF finder with linking length $b = 0.168$.

Individual cluster mass scatter properties due to line of sight effects were then compared to several intrinsic and environmental cluster properties, including triaxiality, planarity of filament or halo mass in the immediate neighborhood of the cluster and relative richness of largest galaxy subgroup within the cluster. For example, pairwise correlations, and their combined effects using PCA, showed that clusters with average mass measurements (over lines of sight) which are large tend to also have large mass scatter around their average, relatively high sphericity and small triaxiality, richness in the largest subgroup, and offset of the galaxy position average from the cluster center. Relations were also seen for other quantities such as concentration, recent major merger time and fraction of halo mass near the cluster within a $3 h^{-1} \text{Mpc}$ plane.

Finally, instead of considering each cluster individually, we considered the sample of all clusters and all lines of sight together, and found that most of the trends for the analysis of $\bar{M}_{\text{est}}/M_{\text{true}}$ remained, albeit at different strengths. The projection on the direction of largest scatter was more weakly correlated with the observation angle relative to the cluster long axis.

It is interesting to think about applying these methods directly to observation. One would need more information, in particular estimates of $M_{\text{true}}(M_{\text{est}})$, rather than the opposite which we have here. This requires calibrations from simulations which better sample an expected observational sample at the high mass end, and which also include estimated masses from lower mass halos (as well as faithfully reproducing the observational systematics and selection function). Such a simulation would provide correlations and covariances and predicted likelihood masses M_{like} (and a variant, M_4 considered above, based on a narrow direction of scatter in our sample). PCA could then be applied to $M_{\text{est}}/M_{\text{like}}$ or M_{est}/M_4 , rather than $M_{\text{est}}/M_{\text{true}}$ as we did here. It would be interesting to see if these PC vectors also had relations to cluster orientation such as we found, or perhaps other quantities such as $M_{\text{like}}/M_{\text{true}}$. They might also give some idea of which follow up mass measurement methods would together provide the most constraining power. One could for example identify the measurement method with potentially the least covariance with measurements already in hand. More generally one could design a combination of measurement methods with smaller covariant scatter (and hopefully smaller scatter as well) using calculated PC vectors as a guide, if the simulations are faithful enough. It

is a major challenge to accurately capture the systematics and selection function of observational surveys with numerical simulations. Another technical issue is to improve estimates of the correlations and covariances, so that sets of inconsistent measurements can be more easily recognized. It would be very interesting to do such analyses on a larger box, and/or with other measurement methods.

ACKNOWLEDGEMENTS

YN thanks E. Rasia for discussions and the Essential Cosmology for the Next Generation school for the opportunity to present results of this work. She was supported in part by NSF. JDC thanks A. Ross for suggestions and M. White for numerous helpful discussions and suggestions. We both thank Z. Lukic, E. Rozo and the anonymous referee for extremely helpful criticisms and comments on the draft.

REFERENCES

- Abell G.O., 1958, *ApJS*, 3, 211
- Allen, S., Evrard, A.E., Mantz, A.B., 2011, *ARA&A*, 49, 409
- Angulo, R.E., Springel, V., White, S.D.M., Jenkins, A., Baugh, C.M., Frenk, C.S., 2012, *arXiv:1203.3216*
- Aragón-Calvo, M. A., Jones, B. J. T., van de Weygaert, R., & van der Hulst, J. M., 2007a, *A & A*, 474, 315
- Aragón-Calvo, M.A., Shandarin, S.F., Szalay, A., 2010, *arXiv:1006.4178*
- Aragón-Calvo, M. A., van de Weygaert, R., Jones, B. J. T., 2010, *MNRAS*, 408, 2163
- Bahe, Y.M., McCarthy, I.G., King, L.J., 2012, *MNRAS*, 421, 1073
- Bailin, J., & Steinmetz, M., 2005, *ApJ*, 627, 647
- Barrow, J. D., Bhavsar, S. P., Sonoda, D. H., 1985, *MNRAS*, 216, 17
- Basilakos, S.; Plionis, M.; Yepes, G.; Gottlber, S.; Turchaninov, V., 2006, *MNRAS*, 365, 539
- Battaglia, N.; Bond, J. R.; Pfrommer, C.; Sievers, J. L., 2011, *arXiv:1109.3709*
- Becker, M., Kravtsov, A.V., 2011, *ApJ*, 740, 25
- Benson, B., et al., 2011, *arXiv:1112.5435*
- Biesiadzinski, T.; McMahon, J. J.; Miller, C. J.; Nord, B.; Shaw, L., 2012, *arXiv:1201.1282*
- Biviano, A., Murante, G., Borgani, S., Diaferio, A., Dolag, K., Girardi, M., 2006, *A & A*, 456, 23
- Bond, N., Strauss, M., Cen, R., 2010a, *MNRAS*, 406, 1609
- Bond, N.A., Strauss, M.A., Cen, R., 2010b, *MNRAS*, 409, 156
- Bond J. R., Kofman L., Pogosyan D., 1996, *Nature*, 380, 603
- Borgani, S., 2008, *LNP*, 740, 287
- Ceccarelli, L., Paz, D.J., Padilla, N., Lambas, D.G., 2011, *MNRAS*, 412, 1778
- Cen R., 1997, *ApJ*, 485, 39
- Chambers, S.W., Melott, A.L., Miller, C.J., 2000, *ApJ*, 544, 104
- Cohn, J.D., 2011, *MNRAS*, 419, 1017
- Cohn, J.D., Evrard, A.E., White, M., Croton, D., Ellingson, E., 2007, *MNRAS*, 382, 1738
- Cohn J.D., White M., 2009, *MNRAS*, 393, 393
- Colberg, J., White, S.D.M., Jenkins, A., Pearce, F.R., 1999, *MNRAS*, 308, 593
- Colberg, J., Krughoff, K.S., Connolly, A.J., 2005, *MNRAS*, 359, 272
- Colberg, J. M., 2007, *MNRAS*, 375, 337
- Colombi, S., Pogosyan, D., Souradeep, T., 2000, *PRL* 85, 5515
- Conroy C., Gunn J.E., White M., 2009, *ApJ*, 699, 486
- Conroy C., White M., Gunn J.E., 2010, *ApJ*, 708, 58
- Conroy C., Gunn J.E., 2010, *ApJ*, 712, 833
- Conroy, C., Wechsler, R.H., Kravtsov, A.V., 2006, *ApJ*, 647, 201
- Costa-Duarte, M.V., Sodre Jr., L., Durret, F., 2011, *MNRAS*, 411, 1716
- Cuesta, A. J., Prada, F., Klypin, A., Moles, M., 2008, *MNRAS*, 389, 385
- Dalton, G.B., Efstathiou, G., Maddox, S.J., Sutherland, W.J., 1992, *ApJL* 390, L1
- Davis M., Efstathiou G., Frenk C.S., White S.D.M., 1985, *ApJ*, 292, 371
- den Hartog, R., Katgert, P., 1996, *MNRAS*, 279, 349
- Diemand J., Kuhlen M., Madau P., 2006, *ApJ*, 649, 1
- Dressler A., Shectman S.A., 1988, *AJ*, 95, 985
- Einasto, J., Klypin, A.A., Saar, E., Shandarin, S.F., 1984, *MNRAS*, 206, 529
- Einasto, M., Liivamagi, L.J., Saar, E., Einasto, J., Tempel, E., Tago, E., Martinez, V.J., 2011, *A&A*, 535, 36
- Einasto, M., et al., 2012, *A&A*, 542, A36
- Erickson, B.M.S., Cunha, C.E., Evrard, A.E., 2011, *PRD*, 84, 103506
- Fahlman, G., Kaiser, N., Squires, G., Woods, D., 1994, *ApJ*, 437, 56
- Faltenbacher, A., Gottlöber, S., Kerscher, M., Muller, V., 2002, *A & A*, 395, 1
- Faltenbacher, A., Allgood, B., Gottlöber, S., Yepes, G., Hoffman, Y., 2005, *MNRAS*, 362, 1099
- Feroz, F., Hobson, M.P., 2012, *MNRAS*, 420, 596
- Forero-Romero J.E., Hoffman Y., Gottlöber S., Klypin, A., Yepes G., 2009, *MNRAS*, 396, 1815
- Genovese, C.R., Perone-Pacifico, M., Verdinelli, I., Wasserman, L., 2012, *Journal of the American Statistical Association*, 107, 498
- Gerke, B.F., et al., 2005, *ApJ*, 625, 6
- Gonzalez, R.E., Padilla, N., 2010, *MNRAS*, 407, 1449
- Hahn, O., Porciani, C., Carollo, C. M., Dekel, A., 2007a, *MNRAS*, 375, 489
- Hallman, E.J., O'Shea, B.W., Burns, J.O., Norman, M.L., Harkness, R., Wagner, R., 2007, *ApJ* 671, 27
- Hoekstra H., 2001, *A&A*, 370, 743
- Hoekstra, H., Hartlap, J., Hilbert, S. van Uitert, E., 2011, *MNRAS*, 412, 2095
- Holder, G.P., McCarthy, I.G., Babul, A., 2007, *MNRAS* 382, 1697
- Hopkins, P.F., Bahcall, N., Bode, N., 2004, *ApJ* 618, 1
- Hu, W., Kravtsov, A.V., 2003, *ApJ*, 584, 702
- Jasche, J., Wandelt, B.D., 2012, *arXiv:1203.3639*
- Jeeson-Daniel, A., Dalla Vecchia, C., Haas, M.R., Schaye, J., 2011, *MNRAS Letters*, 415, 69
- Jolliffe, I.T., 2002, *Principal Component Analysis*. Springer Series in Statistics, 2nd Edition, Springer, Berlin
- Kaiser, N., 1995, *ApJL*, 439, 1

- Kasun S.F., Evrard A.E., 2005, *ApJ*, 629, 781
- Koester B.P., et al., 2007, *ApJ*, 660, 221
- Lee, J., Evrard, A.E., 2007, *ApJ* 657, 30
- Lee, J., Springel, V., Pen, U.-L., Lemson, G., 2008, *MNRAS* 389, 1266
- Luki, Z., Reed, D., Habib, S., Heitmann, K., 2009, *ApJ*, 692, 217
- Lumsden, S.L., Nichol, R.C., Collins, C.A., Guzzo, L., 1992, *MNRAS* 258,1
- Mantz, A., Allen, S. W., Ebeling, H., Rapetti, D., Drlica-Wagner, A., 2010, *MNRAS*, 406, 1773
- Marrone, D.P., et al., 2012, *ApJ*, 754, 119
- Mecke, K. R., Buchert, T., Wagner, H., 1994, *A & A*, 288, 697
- Meneghetti, M., Fedeli, C., Pace, F., Gottloeber, S., Yepes, G., 2010, *A&A*, 519, 90
- Metzler C., White M., Loken C., 2001, *ApJ*, 547, 560
- Murphy, D.N.A., Eke, V.R., Frenk, C.S., 2011, *MNRAS*, 413, 2288
- Myers, S.T., et al., 2009, *arXiv:0903.0401*
- Navarro J.F., Frenk C.S., White S.D.M., 1997, *ApJ*, 490, 493
- Noh, Y., Cohn, J.D., 2011, *MNRAS*, 413, 301
- Novikov, D., Colombi, S., Doré, O., 2006, *MNRAS*, 366, 1201
- Onuora, L.I., Thomas, P.A., 2000, *MNRAS*, 319, 614
- Paz, D. J., Stasyszyn, F., Padilla, N. D., 2008, *MNRAS*, 389, 1127
- Paz, D.J., Sgro, M.A., Merchan, M., Padilla, N., 2011, *MNRAS*, 414, 2029
- Pereira, M. J., Bryan, G. L., Gill, S. P. D., 2008, *ApJ*, 672, 825
- Pimblet, K. A., 2005a, *MNRAS*, 358, 256
- Pimblet, K. A., 2005b, *Publications of the Astronomical Society of Australia*, 22, 136
- Pogosyan, D., Pichon, C., Gay, C., Prunet, S., Cardoso, J. F., Sousbie, T., Colombi, S., 2009, *MNRAS*, 396, 635
- de Putter R., White M., 2005, *New Astronomy*, 10, 676
- Ragone-Figueroa, Cinthia; Plionis, Manolis, 2007, *MNRAS*, 377, 1785
- Rasia, E., Meneghetti, M., Martino, R., Borgani, S., et al., 2012, *NJPh*, 14, 055018
- Reblinsky K., Bartelmann M., 1999, *A&A*, 345, 1
- Rozo, E., et al., 2009, *ApJ*, 699, 768
- Rozo, E., Rykoff, E., Koester, B., Nord, B., Wu, H.-Y., Evrard, A.E., Wechsler, R., 2011, *ApJ*, 740, 53
- Rykoff, E.S., et al., 2008, *MNRAS Letters*, 387, 28
- Sahni, V., Sathyaprakash, B. S., Shandarin, S. F., 1998, *ApJL*, 495, L5
- Saro, A., Bazin, G., Mohr, J.J., Dolag, K., 2012, *arXiv:1203.5708*
- Schmalzing, J., Buchert, T., Melott, A. L., Sahni, V., Sathyaprakash, B. S., Shandarin, S. F., 1999, *ApJ*, 526, 568
- Shandarin, S.F., Zel'dovich, Ia. B., 1983, *Comments on Astrophysics*, 10, 33
- Shandarin, S., Habib, S., Heitmann, K., 2012, *PhRvD*, 85, 083005
- Shandarin, S., 2010, *JCAP*, 5, 015
- Shaw, L.D., Holder, G.P., Bode, P., 2008, *ApJ*, 686, 206
- Sheth, J.V., Sahni, V., Shandarin, S.F. & Sathyaprakash, B., 2003, *MNRAS*, 343, 22
- Skibba, R. A., Sheth, R.K., 2009, *MNRAS* 392, 1080
- Skibba, R. A., Maccio, A.V., 2011, *MNRAS*, 416, 2388
- Smith, A. G., Hopkins, A. M., Hunstead, R. W., Pimblet, K. A., 2012, *MNRAS*, 422, 25
- Sousbie, T., Pichon, C., Colombi, S., Novikov, D., Pogosyan, D., 2008b, *MNRAS*, 383, 1655
- Sousbie, T., Colombi, S., Pichon, C., 2009, *MNRAS*, 393, 457
- Sousbie, T., 2010, 2011, *MNRAS*, 414, 350
- Stanek, R., Rasia, E., Evrard, A.E., Pearce, F., Gazzola, L., 2010, *MNRAS*, 403, 1072
- Stoica, R. S., Martínez, V. J., Mateu, J., Saar, E., 2005, *A & A*, 434, 423
- Stoica, R. S., Martinez, V. J., Saar, E., 2007, *JRSSC*, 56, 459
- Stoica, R.S., Martinez, V.J., Saar, E., 2010, *A&A*, 510, 38
- Splinter, R.J., Melott, A. L., Linn, A., Buck, C., Tinker, J., 1997, *ApJ*, 479, 632
- Sunyaev R. A. & Zel'dovich, Ya. B., 1972, 1972, *Comm. Astrophys, Space Phy.*, 4, 173
- Sunyaev R. A. & Zel'dovich, Ya. B., 1980, *ARA&A*, 18, 537
- Tormen G., 1997, *MNRAS*, 290, 411
- van Haarlem M.P., Frenk C.S., White S.D.M., 1997, *MNRAS*, 287, 817
- van de Weygaert, R., Bertschinger, E., 1996, *MNRAS*, 281, 84
- van de Weygaert, R., 2002, *Proceedings 2nd Hellenic Cosmology Workshop*, eds. M. Plionis, S. Cotsakis, I. Georgantopoulos, Kluwer, astro-ph/0206427
- van de Weygaert, R., Schaap, W., 2007, *arXiv:0708.1441*
- Voit, G.M., 2005, *Rev. Mod. Phys.* 77, 207
- Way, M.J., Gazis, P.R., Scargle, J.D., 2011, *ApJ*, 727, 48
- Wetzel, A.R., Cohn, J.D., White, 2009, *MNRAS*, 395, 1376
- Wetzel, A.R., White, M., 2010, *MNRAS*, 403, 1072
- White, R. A., Bliton, M., Bhavsar, S. P., Bornmann, P., Burns, J. O., Ledlow, M. J., Loken, C., 1999, *AJ*, 118, 2014
- White M., 2001, *A&A*, 367, 27
- White, M., Hernquist, L., Springel, V., 2002, *ApJ*, 579, 16
- White M., 2002, *ApJS*, 143, 241
- White, M., Cohn, J.D., Smit, R., 2010, *MNRAS*, 408, 1818
- Wojtak, R., Lokas, E.L., Mamon, G.A., Gottlober, S., Prada F., Moles M., 2007, *A&A* 466, 437
- Wu, Y., Batuski, D.J., Khalil, A., 2009, *ApJ* 707, 1160
- Yang, H.-Y. Karen, Bhattacharya, S., Ricker, P.M., 2010, *ApJ*, 725, 1124
- Yang X., Mo H.J., van den Bosch F.C., Pasquali, A., Li, C., Barden, M., 2007, *ApJ*, 671, 153
- Zel'dovich, Ia.B., Einasto, J., Shandarin, S.F., 1982, *Nature*, 300, 407
- Zhang, Y., Yang, X., Faltenbacher, A., Springel, V., Lin, W., Wang, H., 2009, *ApJ*, 706, 747